JOURNAL OF SPACECRAFT AND ROCKETS
Vol. 46, No. 3, May–June 2009

Asteroid Diversion Using a Long Tether and Ballast

David B. French* and Andre P. Mazzoleni†
North Carolina State University, Raleigh, North Carolina 27695

DOI: 10.2514/1.40828

The threat of an asteroid or comet impacting the Earth has been receiving more attention in recent years, due in part to the discovery of the Apophis asteroid, which was at one time projected to have a significant probability of impacting the Earth in the year 2029. Although a later analysis of the Apophis trajectory precluded this impact, the threat has brought a lot of attention to the dangers posed by asteroids. Many ideas have been put forward for mitigating such threats. This paper presents one such technique: the attachment of a long tether and ballast mass to change the orbit of an Earth-threatening asteroid or comet. Specifically, for this paper, a parametric study was conducted to determine to what degree the trajectory of an asteroid or comet could be altered by attaching a tether and ballast for various values of orbital semimajor axis and eccentricity and for various tether lengths and ballast mass sizes. The results show that a long tether and ballast mass could be effective for such a diversion. It was found that the technique was most effective using longer tethers and larger ballast masses on asteroids or comets with smaller, more eccentric, orbits.

Nomenclature

a	=	orbit semimajor axis, astronomical units (AU)
$\mathbf{a}_{A/O}$	=	acceleration of point A with respect to point O, km/s^2
$\mathbf{a}_{B/O}$	=	acceleration of point B with respect to point O, km/s^2
a_i	=	MATLAB ordinary differential equation suite absolute error for the ith component of the state vector
$\mathbf{a}_1$	=	first unit vector in A frame
$\mathbf{a}_2$	=	second unit vector in A frame
$\mathbf{a}_3$	=	third unit vector in A frame
$\mathbf{b}_1$	=	first unit vector in body frame
$\mathbf{b}_2$	=	second unit vector in body frame
$\mathbf{b}_3$	=	third unit vector in body frame
E_i	=	MATLAB ordinary differential equation suite allowable estimated error
e	=	orbit eccentricity
$\mathbf{e}_1$	=	first unit vector in the inertial frame
$\mathbf{e}_2$	=	second unit vector in the inertial frame
$\mathbf{e}_3$	=	third unit vector in the inertial frame
F_{GA}	=	force of gravity of point A, kN
F_{GB}	=	force of gravity of point B, kN
f_{B1}	=	arbitrary force on B in the $\mathbf{b}_1$ direction, kN
f_{B2}	=	arbitrary force on B in the $\mathbf{b}_2$ direction, kN
K	=	function for compression of equations of motion, s^{-1}
L	=	tether length, km
$\tilde{m}$	=	ballast to the near-Earth object's mass ratio
m_A	=	near-Earth object's mass, kg
m_B	=	ballast mass, kg
R	=	scalar distance between the sun and near-Earth objects, km
$\mathbf{R}_{A/O}$	=	vector from point O to point A, km
R_B	=	scalar distance from the sun to point B, km
$\mathbf{R}_{B/A}$	=	vector from point A to point B, km
R_E	=	mean Earth radius, 6378.137 km
R_{ref}	=	scalar distance from the sun to reference point on the reference orbit, km
r	=	MATLAB ordinary differential equation suite relative error
t_{end}	=	simulation duration, years
$\mathbf{v}_{A/O}$	=	velocity of point A with respect to point O, km/s
$\mathbf{v}_{B/O}$	=	velocity of point B with respect to point O, km/s
y_i	=	MATLAB ordinary differential equation suite state vector component
γ	=	angle between the directions of tension and gravity force on point A, rad
Δ	=	scalar distance between unattached near-Earth objects and attached near-Earth objects, R_E
$\Delta\epsilon$	=	change in specific mechanical energy, m^2/s^2
δ	=	angle between the directions of tension and gravity force on point B, rad
δR	=	scalar difference between distance to the actual point and reference point, km
$\delta\nu$	=	difference between true anomalies of the actual point and reference point, rad
ϵ	=	specific mechanical energy, m^2/s^2
ϵ_1	=	specific mechanical energy of the unattached system, m^2/s^2
ϵ_2	=	specific mechanical energy of the attached system, m^2/s^2
θ	=	tether angle, rad
θ_i	=	initial value of θ, rad
λ	=	mass center offset parameter, product of $\tilde{m}$ and L, km
μ_{sun}	=	gravitational parameter of the sun, 1.327×10^{11} km^3/s^2
ν	=	true anomaly, rad
ν_{ref}	=	true anomaly of the reference point on the reference orbit, rad

Received 5 September 2008; revision received 21 January 2009; accepted for publication 9 February 2009.

*Ph.D. Student, Mechanical & Aerospace Engineering. Student Member AIAA.

†Associate Professor, Mechanical & Aerospace Engineering. Associate Fellow AIAA.

I. Introduction

OVER the course of history, the Earth has experienced many impacts of asteroids and comets, collectively referred to in this paper as near-Earth objects (NEOs). The evidence of these impacts exists in the geological evidence of craters, such as the 1.2-km-diam Arizona impact crater, which was formed approximately 50,000 years ago [1]; the 180-km-diam Chicxulub crater on the north coast of the Yucatan Peninsula, which is hypothesized to have resulted from a meteor impact about 65 million years ago [2]; and the even larger 300-km-diam Vredefort crater in South Africa, which is 2 billion years old and the largest known impact crater on the Earth [3].

Recently, the threat of future NEO impacts on the Earth has gained increased attention. On 27 December 2004, the asteroid Apophis was projected to have a 1-in-38 chance of striking the Earth in 2029 [4].

This impact was ruled out a day later, but the publicity from this event, combined with the potential impact risk of a resonant encounter in 2036, served to awaken the public to the risk posed by NEOs, leading Congress to call on NASA to investigate mitigation alternatives [5].

The question of how to alter the trajectory of such a threat has been the subject of much research. Several mitigation techniques have been proposed, including detonating nuclear or conventional explosives in, on, or near the NEO [6], guiding a retrograde NEO to impact the Earth-threatening NEO [7], taking advantage of the Yarkovsky effect [8], or using a tug of some type, whether connected to the NEO [9] or using gravity to pull the NEO [10].

This paper takes a different approach: rendezvous with and attachment of a long tether and ballast mass to a NEO. This is not to be confused with the method proposed by Chobotov [11], a diversion approach using a relatively short tether. The tether–ballast system attachment proposed in this paper would affect the trajectory of the NEO in two ways. First, the connection of a tether and ballast mass would instantaneously change the center of mass of the system and therefore the orbit. Second, the tether tension would add a perturbing force that would also change the NEO's trajectory.

II. Model

It is desirable to determine how effectively a tether and ballast mass could alter the trajectory of a NEO. To accomplish this task, a numerical parametric study was conducted using MATLAB [12] to determine the change in the trajectory of a NEO due to tether and ballast attachments, in which several initial conditions were varied, including orbital elements (the semimajor axis a and the eccentricity e) and physical characteristics (length of the tether L and the ballast-to-NEO mass ratio $\tilde{m}$) of the NEO–tether–ballast system. The latter parameter is defined in Eq. (1), in which m_B is the mass of the ballast and m_A is the mass of the NEO:

$$\tilde{m} = \frac{m_B}{m_A} \tag{1}$$

The goal of this study was to determine the extent to which a tether and ballast mass system alone would change the trajectory of threatening NEOs: specifically, NEOs of the Aten and Apollo NEO groups[‡] (both Earth-orbit-crossing). To this end, a simplified model of the system was constructed. The only gravitational force allowed to act on the NEO and ballast mass was that of the sun. The only additional force considered was the tether tension. The attachment of the fully extended tether and ballast mass was assumed to occur instantaneously, and this attachment was assumed to neither change the position of the NEO nor to impart any change in momentum to the NEO at the time of attachment. Therefore, the center of mass of the unattached NEO differed from the center of mass of the NEO–tether–ballast system. This change in the center of mass of the system was the dominant factor in changing the orbit of the NEO, with the acceleration due to the tether tension adding a secondary trajectory deviation (note that further perturbation effects, such as vibrational and librational motion [13], might further add to the trajectory alteration, but are not included in this study). The tether itself was assumed to be massless, inextensible, and of constant length. Additionally, all masses were assumed to be point masses, and all motion was constrained to the plane of the Earth's orbit about the sun.

The system can be seen in Fig. 1. In this figure, there are three reference frames established. The three unit vectors $\{\mathbf{e}_1, \mathbf{e}_2, \mathbf{e}_3\}$ comprise the inertial frame. The $\{\mathbf{a}_1, \mathbf{a}_2, \mathbf{a}_3\}$ frame rotates such that $\mathbf{a}_1$ is always aligned with $\mathbf{R}_{A/O}$ and $\mathbf{a}_3$ remains aligned with $\mathbf{e}_3$. The $\{\mathbf{b}_1, \mathbf{b}_2, \mathbf{b}_3\}$ frame is the body frame of the NEO–tether–mass system and rotates such that $\mathbf{b}_1$ is always aligned with $\mathbf{R}_{B/A}$ and $\mathbf{b}_3$ remains aligned with $\mathbf{e}_3$. There are a number of variables that appear in the figure as well. R is the scalar distance from the sun to the NEO, ν is the true anomaly, which is the angle between the periapsis direction

[‡]Data available online at http://neo.jpl.nasa.gov [retrieved 22 April 2008].

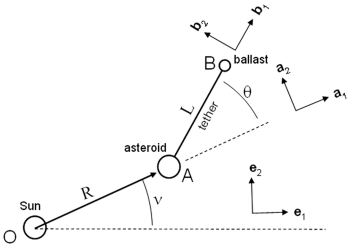

Fig. 1 Diagram of NEO–tether–ballast system.

(same as inertial unit vector $\mathbf{e}_1$) and $\mathbf{R}_{A/O}$, L is the scalar length of the tether, and θ is the angle between the directions of $\mathbf{R}_{A/O}$ and $\mathbf{R}_{B/A}$.

A. Derivation of Equations of Motion

For some of the cases presented in this study, direct integration of the equations of motion (Cowell's method [14]) led to satisfactory results. However, many cases required better convergence than direct integration could provide, due to the stiffness of the equations of motion. To address this, a special perturbation method (specifically, a polar coordinate form of Encke's method [14]) was employed. The Encke's method model can only be understood completely after a derivation of the equations of motion for use with Cowell's method is completed. Therefore, the Cowell's method derivation will be presented in its entirety first, followed by the Encke's method model.

1. Cowell's Method

To begin the derivation, the vectors that determine the positions of the NEO and the ballast mass are defined:

$$\mathbf{R}_{A/O} = R\mathbf{a}_1 \tag{2}$$

$$\mathbf{R}_{B/O} = R\mathbf{a}_1 + L\mathbf{b}_1 \tag{3}$$

Differentiating Eq. (2) with respect to time in the inertial frame yields the velocity of the NEO ($\mathbf{v}_{A/O}$) expressed here in the A frame. Note that all rates in this derivation are with respect to the inertial frame unless otherwise noted:

$$\mathbf{v}_{A/O} = \dot{R}\mathbf{a}_1 + R\dot{\nu}\mathbf{a}_2 \tag{4}$$

Similarly, the differentiation of Eq. (3) in the inertial frame yields the velocity of the ballast ($\mathbf{v}_{B/O}$), expressed here in the B frame:

$$\mathbf{v}_{B/O} = [\dot{R}\cos\theta + R\dot{\nu}\sin\theta + \dot{L}]\mathbf{b}_1 + [-\dot{R}\sin\theta + R\dot{\nu}\cos\theta + L(\dot{\nu} + \dot{\theta})]\mathbf{b}_2 \tag{5}$$

Next, Eqs. (4) and (5) are differentiated again with respect to time to determine the accelerations of the NEO ($\mathbf{a}_{A/O}$) and ballast mass ($\mathbf{a}_{B/O}$):

$$\mathbf{a}_{A/O} = [\ddot{R} - R\dot{\nu}^2]\mathbf{a}_1 + [2\dot{R}\dot{\nu} + R\ddot{\nu}]\mathbf{a}_2 \tag{6}$$

$$\mathbf{a}_{B/O} = [\ddot{R}\cos\theta + 2\dot{R}\dot{\nu}\sin\theta + R\ddot{\nu}\sin\theta + \ddot{L} - R\dot{\nu}^2\cos\theta - L(\dot{\nu} + \dot{\theta})^2]\mathbf{b}_1 + [-\ddot{R}\sin\theta + 2\dot{R}\dot{\nu}\cos\theta + R\ddot{\nu}\cos\theta + 2\dot{L}(\dot{\nu} + \dot{\theta}) + L(\ddot{\nu} + \ddot{\theta}) + R\dot{\nu}^2\sin\theta]\mathbf{b}_2 \tag{7}$$

To form the complete equations of motion using Newton's second law of motion, the forces acting on the end bodies must be determined.

The forces in Fig. 2 include the tether tension force T, which acts in equal magnitude on the NEO and the ballast. F_{GA} is the force of the sun's gravity acting on the NEO, and F_{GB} is the gravity force acting on the ballast. The forces f_{B1} and f_{B2} are miscellaneous forces on the

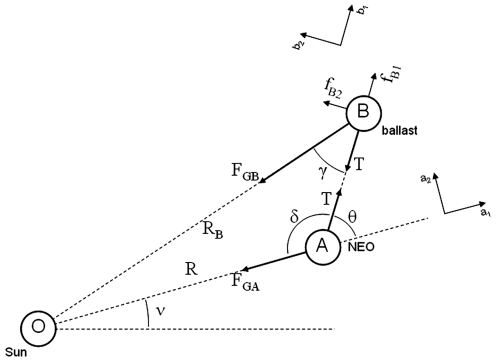

Fig. 2 Diagram of system forces.

ballast mass (for this study, these forces were set equal to zero). The angles δ and γ are used to help orient the force terms and will be related to other variables later in this derivation and therefore do not appear in the final equations of motion. R and R_B are the scalar distances from the sun to the NEO and ballast mass, respectively. The relationship between these forces and the accelerations derived in Eqs. (6) and (7) are expressed here:

$$(T\cos\theta - F_{GA})\mathbf{a}_1 + T\sin\theta\mathbf{a}_2 = m_A\mathbf{a}_{A/O} \tag{8}$$

$$(f_{B1} - T - F_{GB}\cos\gamma)\mathbf{b}_1 + (f_{B2} + F_{GB}\sin\gamma)\mathbf{b}_2 = m_B\mathbf{a}_{B/O} \tag{9}$$

It is possible to express the sine and cosine of the angle γ in terms of defined variables using the law of sines and the law of cosines. These expressions are given in Eqs. (10) and (11):

$$\sin\gamma = \frac{R\sin\theta}{\sqrt{R^2 + L^2 + 2RL\cos\theta}} \tag{10}$$

$$\cos\gamma = \frac{L + R\cos\theta}{\sqrt{R^2 + L^2 + 2RL\cos\theta}} \tag{11}$$

The sun's gravity force can also be expressed in terms of known constants and our primary variables. The expressions for F_{GA} and F_{GB} are given in Eqs. (12) and (13):

$$F_{GA} = \frac{m_A\mu_{\text{sun}}}{R^2} \tag{12}$$

$$F_{GB} = \frac{m_B\mu_{\text{sun}}}{R^2 + L^2 + 2RL\cos\theta} \tag{13}$$

In these equations, μ_{sun} refers to the gravitational parameter of the sun. Splitting Eq. (8) into the $\mathbf{a}_1$ and $\mathbf{a}_2$ directions and Eq. (9) into the $\mathbf{b}_1$ and $\mathbf{b}_2$ directions and substituting Eqs. (6), (7), and (10–13) into those equations, the following equations are derived:

$$T\cos\theta - m_A\frac{\mu_{\text{sun}}}{R^2} = m_A(\ddot{R} - R\dot{\nu}^2) \tag{14}$$

$$T\sin\theta = m_A(2\dot{R}\,\dot{\nu} + R\ddot{\nu}) \tag{15}$$

$$f_{B1} - T - m_B\frac{\mu_{\text{sun}}(L + R\cos\theta)}{(R^2 + L^2 + 2RL\cos\theta)^{3/2}} = m_B[(2\dot{R}\,\dot{\nu} + R\ddot{\nu})\sin\theta + (\ddot{R} - R\dot{\nu}^2)\cos\theta + \ddot{L} - L(\dot{\nu} + \dot{\theta})^2] \tag{16}$$

$$f_{B2} + m_B\frac{\mu_{\text{sun}}R\sin\theta}{(R^2 + L^2 + 2RL\cos\theta)^{3/2}} = m_B[(-\ddot{R} + R\dot{\nu}^2)\sin\theta + (2\dot{R}\,\dot{\nu} + R\ddot{\nu})\cos\theta + 2\dot{L}(\dot{\nu} + \dot{\theta}) + L(\ddot{\nu} + \ddot{\theta})] \tag{17}$$

To compress Eqs. (16) and (17), it is convenient to introduce a new variable substitution, K, which is defined as follows:

$$K = \frac{\mu_{\text{sun}}}{(R^2 + L^2 + 2RL\cos\theta)^{3/2}} \tag{18}$$

Using this substitution and dividing Eqs. (14) and (15) by m_A and Eqs. (16) and (17) by m_B, the four equations can be written as follows:

$$-\frac{T}{m_A}\cos\theta + \frac{\mu_{\text{sun}}}{R^2} + \ddot{R} - R\dot{\nu}^2 = 0 \tag{19}$$

$$-\frac{T}{m_A}\sin\theta + 2\dot{R}\,\dot{\nu} + R\ddot{\nu} = 0 \tag{20}$$

$$-\frac{f_{B1} + T}{m_B} + K(L + R\cos\theta) + (2\dot{R}\,\dot{\nu} + R\ddot{\nu})\sin\theta + (\ddot{R} - R\dot{\nu}^2)\cos\theta + \ddot{L} - L(\dot{\nu} + \dot{\theta})^2 = 0 \tag{21}$$

$$-\frac{f_{B2}}{m_B} - KR\sin\theta + (-\ddot{R} + R\dot{\nu}^2)\sin\theta + (2\dot{R}\,\dot{\nu} + R\ddot{\nu})\cos\theta + 2\dot{L}(\dot{\nu} + \dot{\theta}) + L(\ddot{\nu} + \ddot{\theta}) = 0 \tag{22}$$

Equations (19) and (20) are nearly in their final form. Solving Eq. (19) for $\ddot{R}$ and Eq. (20) for $\ddot{\nu}$ produces the following equations:

$$\ddot{R} = R\dot{\nu}^2 - \frac{\mu_{\text{sun}}}{R^2} + \frac{T}{m_A}\cos\theta \tag{23}$$

$$\ddot{\nu} = \frac{T}{m_A R}\sin\theta - \frac{2\dot{R}}{R}\dot{\nu} \tag{24}$$

Some additional manipulation of Eqs. (21) and (22) will be required to get them in their final forms. First, Eq. (22) is multiplied by $\sin\theta$ and subtracted from Eq. (21) multiplied by $\cos\theta$:

$$-\frac{f_{B1} + T}{m_B}\cos\theta + \frac{f_{B2}}{m_B}\sin\theta + KL\cos\theta + KR + \ddot{R} - R\dot{\nu}^2 + \ddot{L}\cos\theta - 2\dot{L}(\dot{\nu} + \dot{\theta})\sin\theta - L(\dot{\nu} + \dot{\theta})^2\cos\theta - L(\ddot{\nu} + \ddot{\theta})\sin\theta = 0 \tag{25}$$

Next, Eq. (22) is multiplied by $\sin\theta$ and then *added* to Eq. (21) multiplied by $\cos\theta$:

$$-\frac{f_{B1} + T}{m_B}\sin\theta - \frac{f_{B2}}{m_B}\cos\theta + KL\sin\theta + 2\dot{R}\,\dot{\nu} + R\ddot{\nu} + \ddot{L}\sin\theta + 2\dot{L}(\dot{\nu} + \dot{\theta})\cos\theta - L(\dot{\nu} + \dot{\theta})^2\sin\theta + L(\ddot{\nu} + \ddot{\theta})\cos\theta = 0 \tag{26}$$

By subtracting Eq. (19) from Eq. (25), Eq. (27) is derived:

$$\left[-\frac{f_{B1}}{m_B} + T\left(\frac{1}{m_A} + \frac{1}{m_B}\right) + KL + \ddot{L} - L(\dot{\nu} + \dot{\theta})^2\right]\cos\theta + \left[\frac{f_{B2}}{m_B} - 2\dot{L}(\dot{\nu} + \dot{\theta}) - L(\ddot{\nu} + \ddot{\theta})\right]\sin\theta + KR - \frac{\mu_{\text{sun}}}{R^2} = 0 \tag{27}$$

Subtracting (20) from Eq. (26) results in Eq. (28):

$$\left[-\frac{f_{B1}}{m_B}+T\left(\frac{1}{m_A}+\frac{1}{m_B}\right)+KL+\ddot{L}-L(\dot{\nu}+\dot{\theta})^2\right]\sin\theta + \left[-\frac{f_{B2}}{m_B}+2\dot{L}(\dot{\nu}+\dot{\theta})+L(\ddot{\nu}+\ddot{\theta})\right]\cos\theta=0 \tag{28}$$

Next, Eq. (28) is multiplied by $\cos\theta$ and subtracted from Eq. (27) multiplied by $\sin\theta$ to arrive at another equation of motion in final form:

$$\ddot{\theta}=\frac{1}{L}\left[\frac{f_{B2}}{m_B}-2\dot{L}(\dot{\nu}+\dot{\theta})+\left(KR-\frac{\mu_{\text{sun}}}{R^2}\right)\sin\theta\right]-\ddot{\nu} \tag{29}$$

Finally, Eq. (28) is multiplied by $\cos\theta$ and *added* to Eq. (27) multiplied by $\sin\theta$ to complete the set of equations of motion:

$$\ddot{L}=\frac{f_{B1}}{m_B}-T\left(\frac{1}{m_A}+\frac{1}{m_B}\right)-KL+L(\dot{\nu}+\dot{\theta})^2 + \left(\frac{\mu_{\text{sun}}}{R^2}-KR\right)\cos\theta \tag{30}$$

Equations (23), (24), (29), and (30) comprise the full system of equations necessary to numerically simulate the NEO–tether–ballast system. However, direct numerical integration (Cowell's method) of these equations can be problematic, due to large order-of-magnitude variances between the variables and the limitations of machine precision (for more details, see Appendix A). Therefore, it is desirable to find another method of simulating the system (other than direct integration), as will be discussed subsequently.

2. *Encke's Method*

Although Cowell's method involves numerically integrating all system accelerations, with Encke's method, only the perturbing accelerations are integrated [14]. These results are then added to a Keplerian (i.e., untethered) reference orbit. This sum provides all necessary information to determine the actual position of the NEO. Figure 3 illustrates how this scheme works. The reference orbit is elliptical and is determined by the initial conditions of the NEO's position and velocity vectors. At the beginning of the simulation (arbitrarily shown in the figure at perihelion), there is no variation between the Keplerian orbit and the actual orbit. As time goes on, the difference between these orbits will increase. Over time, if the variation Δ between the actual and reference position increases to an unacceptable degree, a new reference orbit can be established based on the current position and velocity of the NEO at that time. Classically, Encke's method has been employed using a Cartesian coordinate system. It is convenient for this study, however, to employ a polar coordinate system.

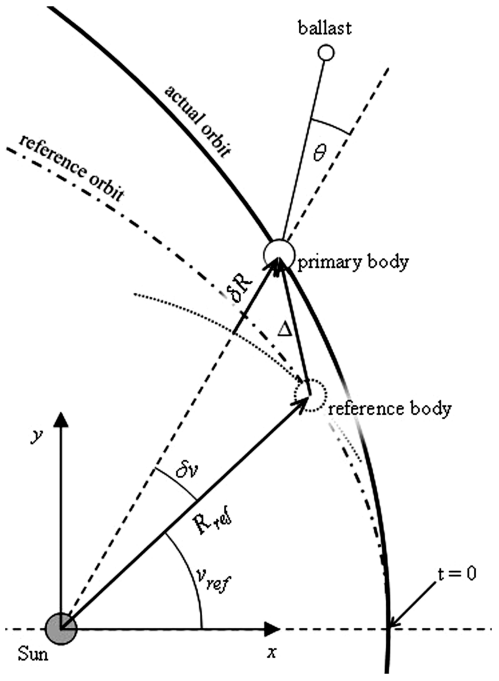

Fig. 3 Diagram of an orbit and reference orbit for use with Encke's method.

In Fig. 3, R_{ref} is the scalar distance from the sun to the reference body, δR is the variation between R_{ref} and the scalar distance to the NEO, reference true anomaly ν_{ref} is the angle from perihelion to the reference body, $\delta\nu$ is the variation between this and the actual true anomaly, and θ is the angle between the local vertical (at the NEO) and the tether.

Mathematically, the variation of the actual NEO position from the reference position is determined by subtracting Keplerian orbital equations from the equations of motion for R [Eq. (23)] and ν [Eq. (24)] derived previously and integrating the resulting equations over time.

The variations between the actual and reference positions can be described as follows:

$$R=R_{\text{ref}}+\delta R \tag{31}$$

$$\nu=\nu_{\text{ref}}+\delta\nu \tag{32}$$

Differentiating these equations twice with respect to time yields the following:

$$\ddot{R}=\ddot{R}_{\text{ref}}+\delta\ddot{R} \tag{33}$$

$$\ddot{\nu}=\ddot{\nu}_{\text{ref}}+\delta\ddot{\nu} \tag{34}$$

These expressions can be rewritten as follows:

$$\delta\ddot{R}=\ddot{R}-\ddot{R}_{\text{ref}} \tag{35}$$

$$\delta\ddot{\nu}=\ddot{\nu}-\ddot{\nu}_{\text{ref}} \tag{36}$$

The equations of motion in vector form for a Keplerian orbit are as follows [14]:

$$\ddot{\mathbf{R}}_{\text{ref}}+\frac{\mu}{R^3}\mathbf{R}_{\text{ref}}=0 \tag{37}$$

Expressing these equations in polar form leads to the following expressions:

$$\ddot{R}_{\text{ref}}=R_{\text{ref}}\dot{\nu}_{\text{ref}}^2-\frac{\mu_{\text{sun}}}{R_{\text{ref}}^2} \tag{38}$$

$$\ddot{\nu}_{\text{ref}}=-\frac{2\dot{R}_{\text{ref}}}{R_{\text{ref}}}\dot{\nu}_{\text{ref}} \tag{39}$$

By combining Eq. (35) with Eqs. (23) and (38), the first Encke equation of motion is derived:

$$\delta\ddot{R}=(R_{\text{ref}}+\delta R)(2\dot{\nu}_{\text{ref}}\delta\dot{\nu}+\delta\dot{\nu}^2)+\delta R\dot{\nu}_{\text{ref}}^2 + \mu_{\text{sun}}\left[\frac{2R_{\text{ref}}\delta R+\delta R^2}{R_{\text{ref}}^2(R_{\text{ref}}+\delta R)^2}\right]+\frac{T}{m_A}\cos\theta \tag{40}$$

Similarly, by combining Eq. (36) with Eqs. (24) and (39), the second Encke equation of motion is derived:

$$\delta\ddot{v} = \frac{-2(\dot{R}_{\text{ref}} + \delta\dot{R})}{R_{\text{ref}} + \delta R}(\dot{v}_{\text{ref}} + \delta\dot{v}) + \frac{2\dot{R}_{\text{ref}}}{R_{\text{ref}}}\dot{v}_{\text{ref}} + \frac{T}{(R_{\text{ref}} + \delta R)m_A}\sin\theta \tag{41}$$

These two equations, along with the equations for $\ddot{\theta}$ [Eq. (29)] and $\ddot{L}$ [Eq. (30)] are the four equations of motion necessary for the numerical simulation of the system using Encke's method. Reference orbit position information is available explicitly, given the current time and the time since perihelion passage.

B. Constraints

The tether in this study was assumed to be of constant length. Given this constraint, $\dot{L}$ and $\ddot{L}$ must both be equal to zero. Additionally, it is assumed that no external forces are acting on the ballast mass, and therefore f_{B1} and f_{B2} are also equal to zero. These assumptions change Eq. (29) as follows:

$$\ddot{\theta} = \frac{1}{L}\left(KR - \frac{\mu_{\text{sun}}}{R^2}\right)\sin\theta - \ddot{v} \tag{42}$$

Equation (30) changes to Eq. (43) when the assumptions are applied:

$$\ddot{L} = 0 = -T\left(\frac{1}{m_A} + \frac{1}{m_B}\right) - KL + L(\dot{v} + \dot{\theta})^2 + \left(\frac{\mu_{\text{sun}}}{R^2} - KR\right)\cos\theta \tag{43}$$

This expression then leads to the expression for determining the tether tension, which can be seen in Eq. (44):

$$\frac{T}{m_A} = \frac{\tilde{m}}{1 + \tilde{m}}\left[-KL + L(\dot{v} + \dot{\theta})^2 + \left(\frac{\mu_{\text{sun}}}{R^2} - KR\right)\cos\theta\right] \tag{44}$$

Equation (42) can either be paired with Eqs. (23) and (24) and integrated with Cowell's method or paired with Eqs. (40) and (41) and integrated using Encke's method. The tether tension over time is required by both methods, and Eq. (44) provides that information.

C. Verification

Comparing the convergence of Encke's method with that of Cowell's method, it can be seen that Encke's method convergences to the solution more rapidly (see Appendix A for details). To verify that our implementation of Encke's method is valid, we compare our results using Encke's method with those obtained for Cowell's method for a semimajor axis of 2 AU (we chose this semimajor axis because the Cowell method converged nicely for this case). This comparison can be seen in Fig. 4 and shows that over a 5-year span, the scalar difference in asteroid position between the two simulations is less than 30 m, which is remarkable given that the asteroid covers a distance of several hundred million kilometers during the course of the simulation. Additionally, Fig. 5 shows the final position of the tether, simulated using the two methods. Note that the positions are essentially identical. The close agreement of the Encke results with the Cowell results, as illustrated by Figs. 4 and 5, serve to establish the validity of the form of Encke's method derived and used in this paper.

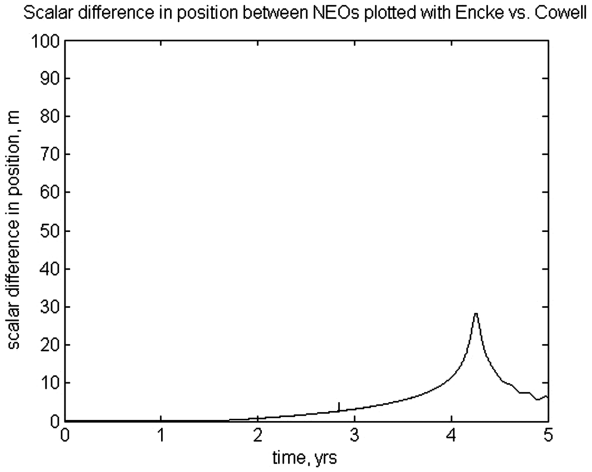

Fig. 4 Scalar difference in position over 5 years between NEOs simulated using Cowell's method (direct integration) and Encke's method. Both NEOs shared the common parameters $\tilde{m} = 0.1$, $L = 100,000$ km, $a = 2$ AU, and $e = 0.8$.

D. Trajectory Alteration

The trajectory of the NEO is changed due to the attachment of the tether and ballast mass. As stated before, this change is due to both the change in system mass center and the perturbative force from the tether tension. As a measure of the effectiveness of the tether and ballast system, the scalar distance Δ between the untethered NEO and the NEO–tether–ballast system was determined as a function of time. This distance was found by comparing numerically simulated trajectories of both an attached and unattached NEO (see Fig. 6). Note that a large value of Δ would not guarantee that an Earth-threatening object would miss Earth. Again, this metric is just a measure of effectiveness for how much the tether and ballast will alter the position of the NEO.

III. Numerical Simulation

To determine the separation distance between the tethered and untethered NEOs, both cases had to be simulated and then compared. For the untethered NEO, the results could be determined by orbit projection based on its known elliptical path, assuming it followed

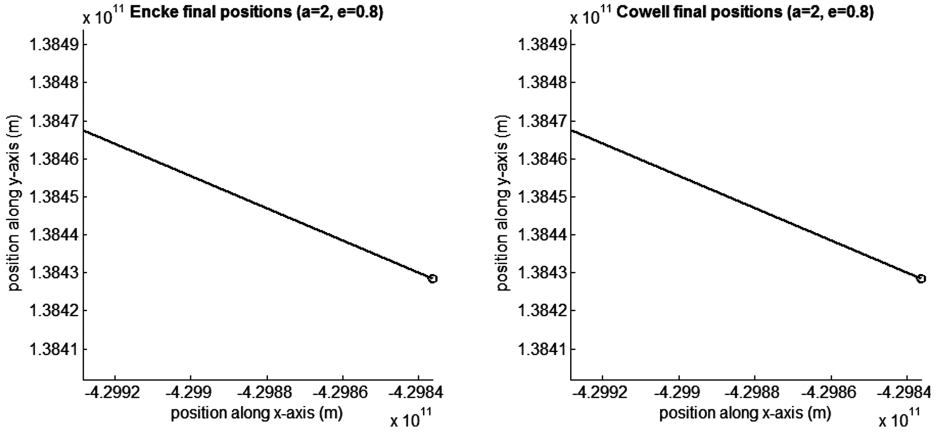

Fig. 5 Final positions of tether after 5 years, simulated using Cowell's method (direct integration) and Encke's method. NEOs shared common parameters $\tilde{m} = 0.1$, $L = 100,000$ km, $a = 2$ AU, and $e = 0.8$.

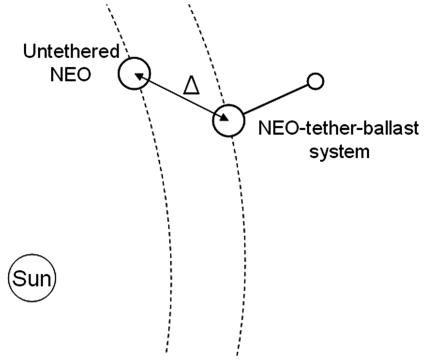

Fig. 6 Definition of the separation distance metric Δ.

the restricted two-body equations of motion [14]. For the NEO–tether–ballast system, the results were generated using numerical simulation via a special perturbation method (specifically, a modified form of Encke's method [14]), as described earlier. As stated in the derivation of equations of motion, this perturbation method was necessary due to convergence issues that arose with attempts at using direct integration (for more discussion on convergence, see Appendix A).

For each simulation, physical parameters and initial conditions were defined. The parameters included the duration t_{end} (most cases presented in this study are 10-year cases), the ballast-to-NEO mass ratio $\tilde{m}$, and the tether length L. The initial conditions included the initial semimajor axis, eccentricity, and true anomaly (a, e, and ν) of the NEO just before tether and ballast attachment. Also included were the initial tether angle θ and the initial tether rotation rate $\dot{\theta}$.

When studying the effect of changing each parameter, it is helpful to specify a baseline set of parameters that will be used in these comparisons. First, the baseline ratio between the ballast mass and the NEO mass will be 1:1000. This value is based on the approximate mass of known potentially hazardous asteroids (PHAs) (see footnote [‡]). Specifically, this would allow a ballast roughly equal in mass to a fueled Saturn V rocket to be used for the smallest known PHA and allow relatively small multiples of this mass to be effective for a large number of PHAs. The baseline tether length will be 10,000 km. This length was deemed to be reasonable based on the ongoing studies on the space elevator concept, which would require a tether roughly 4–10 times as long. The baseline orbital parameters were a semimajor axis of 1.2 AU and an eccentricity of 0.8. These values were chosen because they are central to the parametric space in which this method obtains favorable results. The baseline true anomaly for the tether–ballast attachment was perihelion. The baseline tether angle and angular rate were both set to zero. See Table 1 for a summary of these parameters.

IV. Results

Because the primary result of interest from this study is the diversion of the NEO, the focus of this section will be on determining the scalar distance Δ between the tethered and untethered NEOs, a distance that will be expressed in terms of Earth radii R_E. The reader should note in examining these distances that the NASA analysis of alternatives presented to Congress in 2007 [5] (page 22) indicates that one Earth radius is a sufficient NEO deflection. Specifically, this study will initially involve examining the effect of changing each study parameter on separation distance. The focus will then shift to the rate of change of this separation distance, which will enable a summary of the results that can be applied over any time frame.

A. Effect of Duration

Figure 7 shows the scalar distance between the attached and unattached NEOs over time for a particular case. Note that this distance oscillates as the two systems travel through the orbit. The distance is at a maximum at perihelion and at a minimum at aphelion. However, if a particular true anomaly is chosen (chosen true anomaly represented by circles on figure), the effect is shown to be generally linear over time with respect to the chosen value of true anomaly. That is, the displacement Δ of the tethered NEO position from its untethered position increases approximately linearly with respect to this specified true anomaly.

This phenomenon, though shown for a particular case, is representative of the general case within limits that will be discussed subsequently. Note that the true anomaly chosen for all examples in this paper, unless otherwise specified, corresponds to the true anomaly at which the orbit of the NEO intersects the Earth's orbit as the NEO approaches perihelion.

The curvature of the orbit eventually limits the region of approximate linearity of the slopes as the two systems separate over time. As the tethered and untethered bodies move increasingly further apart, the curvature of the orbit begins to increasingly affect the separation distance. This effect will be seen sooner for cases in which the mass ratio is large or the tether is very long or both. Figure 8 shows an extreme case using a 100,000 km tether and mass ratio of 0.1 (ballast is one-tenth of the NEO mass) shown over 100 years. The figure shows the cyclical nature of the separation distance. This cycling of the separation distance will occur regardless of the parameters chosen.

Ultimately, the maximum separation distance is approximately the average length of the major axes (twice the semimajor axis) of the

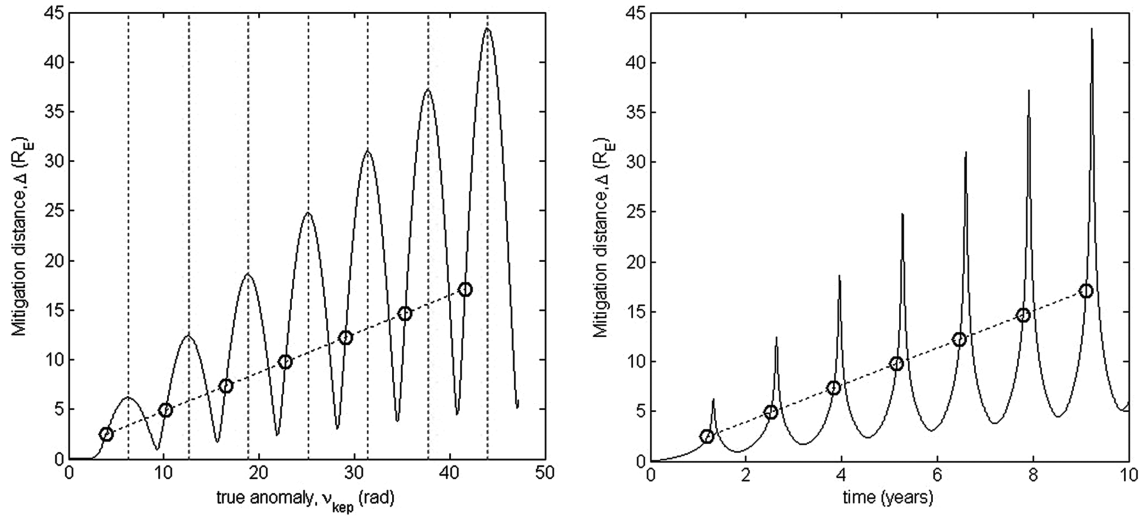

a) **b)**

Fig. 7 Effect of tether mitigation over time shown vs a) true anomaly (angular) scale and b) time scale. All unspecified parameters correspond to the baseline case.

Table 1 Baseline parameters for this study

Parameter	Symbol	Value
Mass ratio	$\tilde{m}$	0.001
Tether length	L	10,000 km
Semimajor axis	a	1.2 AU
Eccentricity	e	0.8
Initial true anomaly	ν_i	0
Initial tether angle	θ_i	0
Initial tether angle rate	$\dot{\theta}_i$	0

two systems, occurring when the tethered and untethered bodies are at opposition with respect to the sun, precisely when one is at periapsis and the other is at apoapsis (Fig. 9). Most cases will take a very long time to reach this maximum separation.

B. Effect of Mass Ratio

By attaching a larger ballast mass to a tether of specified length, the system center of mass is moved in the direction of the ballast mass (this can also be accomplished by increasing tether length). Figure 10 shows the effect of varying the mass ratio. For each case shown, the only varied parameter was the mass ratio, which was varied by an order of magnitude in each successive case. The resulting miss distances correspondingly increased by approximately 1 order of magnitude for each order-of-magnitude increase in the ratio (note the log scale for the ordinate).

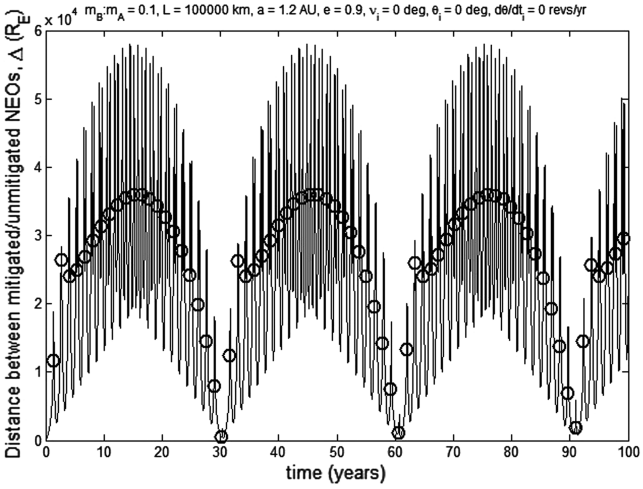

Fig. 8 Effect of duration over time will be cyclical.

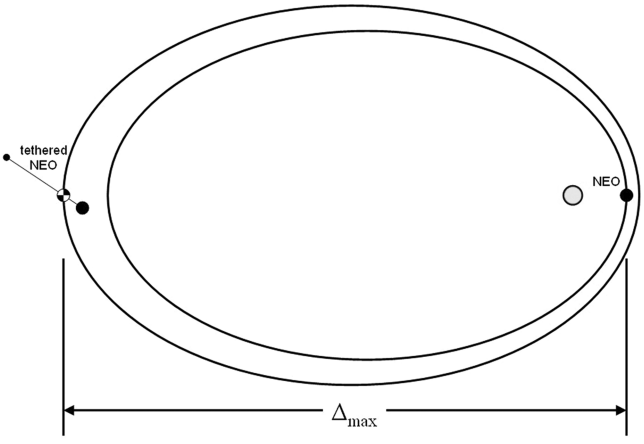

Fig. 9 Maximum separation between tethered and untethered NEOs.

C. Effect of Tether Length

As stated before, changing the tether length is another way to control the degree to which the system center of mass is shifted. Figure 11 shows that, as was the case for the mass ratio, an order-of-magnitude increase in tether length results in an order-of-magnitude increase in miss distance.

Upon comparing Figs. 10 and 11, it can be seen that the effect of changing the tether length is quite similar to that of changing the mass ratio; that is, an increase in tether length results in a proportional increase in Δ. As with changing mass ratio, an order-of-magnitude increase in tether length causes the separation distance to increase by an order of magnitude. Note that the apparent linear regions (though they are not actually linear, due to the logarithmic scale) appearing before the oscillations in Figs. 10 and 11 represent the gradually increasing separation, from an initial separation of zero, between the attached and unattached NEOs before the first periapsis passage. The oscillation itself is a result of the change in separation that occurs over the orbit, with maximums at periapsis and minimums at apoapsis.

Given the nearly equivalent effects of altering the mass ratio $\tilde{m}$ and tether length L, these two parameters will be combined (in a later section) into a single parameter λ to help compress a summary of all results. Specifically, it will be shown in Sec. IV.I that any equivalent product of the mass ratio and the tether length produces a similar result in terms of separation distance. This compression of two parameters will then help to succinctly summarize the results.

D. Effect of Semimajor Axis

Up to this point, the parameters changed have been matters of design choice. The semimajor axis, on the other hand, is a property of the chosen NEO's orbit. It was found that for an orbit with a larger semimajor axis a, the effectiveness of the tether–ballast mitigation technique was reduced. As Fig. 12b shows, a larger semimajor axis results in a lower rate of change of separation distance $\dot{\Delta}$.

The separation rate as a function of semimajor axis is not always monotonic. Figure 13a illustrates how the separation rate relates to the semimajor axis for a variety of eccentricity values. This plot shows that for semimajor axes smaller than approximately 0.75 AU, the rate of separation increases with increasing semimajor axis. For values of semimajor axis greater than 0.75, the separation distance decreases. Recall, however, that these values reflect the true anomaly chosen for slope calculation: at the intersection with Earth's orbit as the NEO approaches perihelion. Figure 13b. shows that if periapsis is chosen as the true anomaly for plotting $\dot{\Delta}$, the rate decreases monotonically with increasing a.

E. Effect of Eccentricity

The eccentricity of the NEO orbit was another parameter studied. Without exception, a more eccentric orbit is more susceptible to trajectory alteration than a less eccentric orbit, assuming that all other parameters remain the same. This can be seen in Fig. 14. In this figure, plotted on a log scale for the y axis, the slope of the separation distance increases as eccentricity increases.

Figure 15 shows that the separation rate increases monotonically with increasing eccentricity, regardless of semimajor axis. Additionally, the two plots, one measuring the effect at an Earth intersecting true anomaly and the other at perihelion, suggest that the relationship is monotonic regardless of the true anomaly at which the rate is measured.

F. Effect of Initial True Anomaly

The true anomaly at which to attach the tether and ballast to a NEO is influential, as Fig. 16 demonstrates. The figure shows that by attaching at perihelion ($\nu = 0$), the effectiveness of the tether–ballast system in altering the position of the NEO over time is maximized. It also shows that the rate is minimized by attaching at aphelion.

Figure 17 gives the separation rates as a function of initial true anomaly for a typical tether–ballast attachment. Starting at 0 deg true anomaly (perihelion), the separation rates are at a maximum.

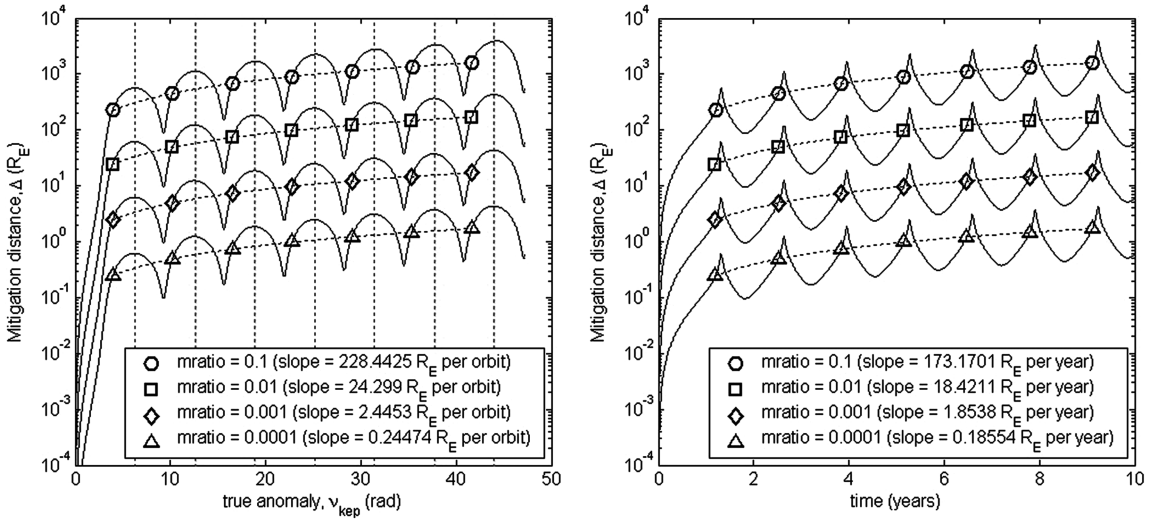

a) b)

Fig. 10 Effect of varying m_A:m_B vs a) true anomaly (angular) scale and b) time scale. All unspecified parameters correspond to the baseline case.

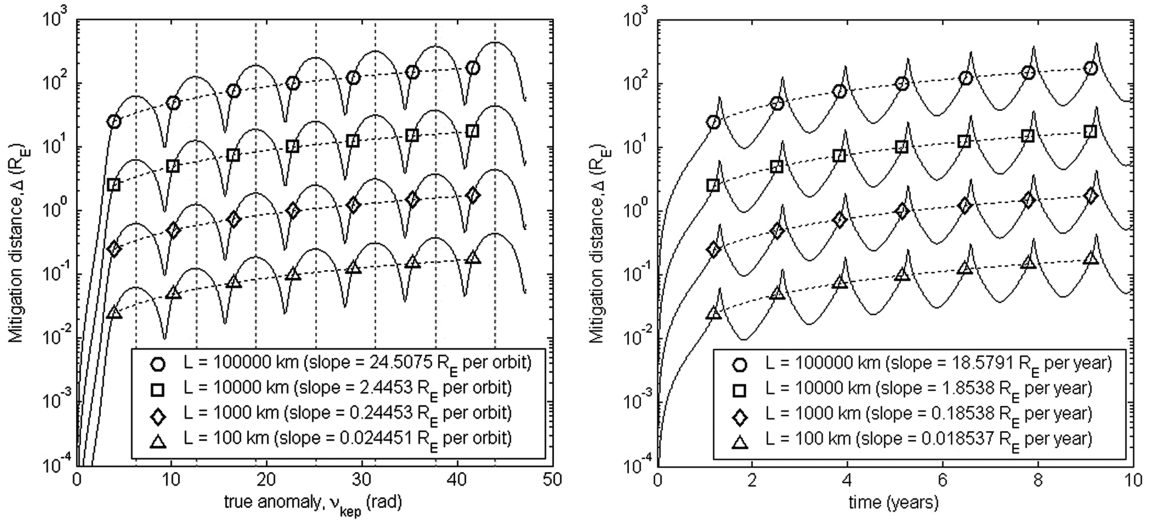

a) b)

Fig. 11 Effect of varying tether length vs a) true anomaly (angular) scale and b) time scale. All unspecified parameters correspond to the baseline case.

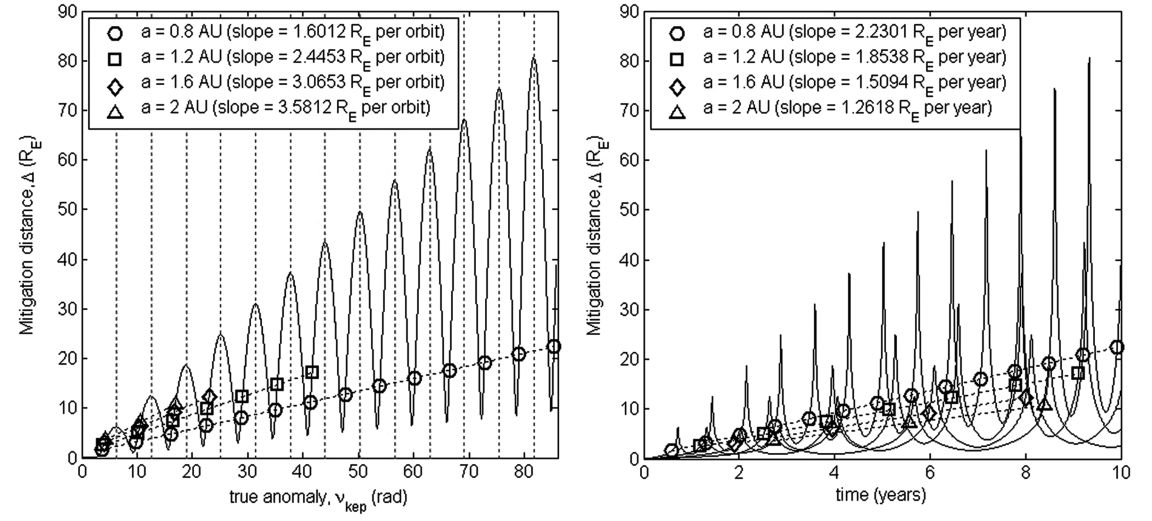

a) b)

Fig. 12 Effect of various orbit semimajor axes vs a) true anomaly (angular) scale and b) time scale.

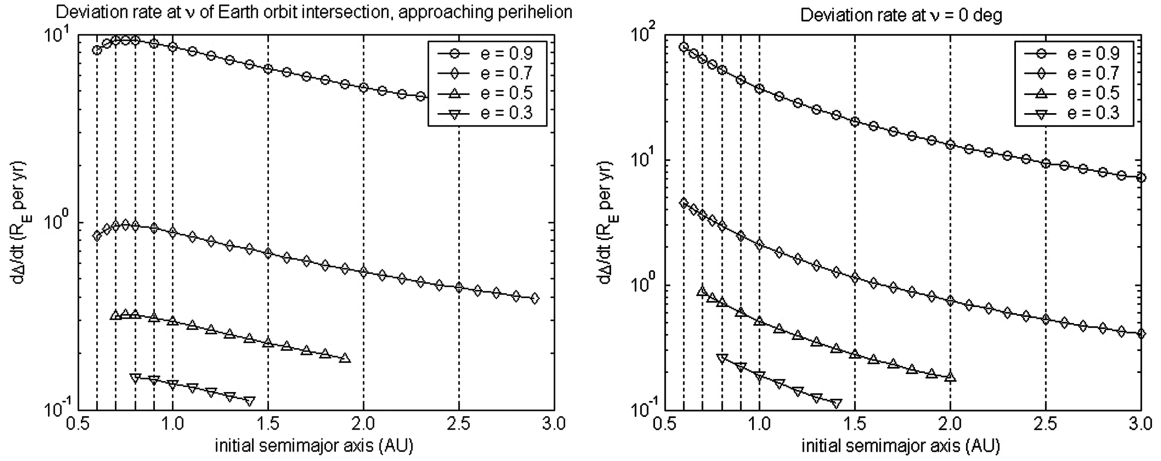

a) b)

Fig. 13 Effect of changing semimajor axis on separation rate of change for a) true anomaly at which NEO orbit intersects Earth orbit approaching perihelion and b) true anomaly at perihelion. All unspecified parameters correspond to the baseline case.

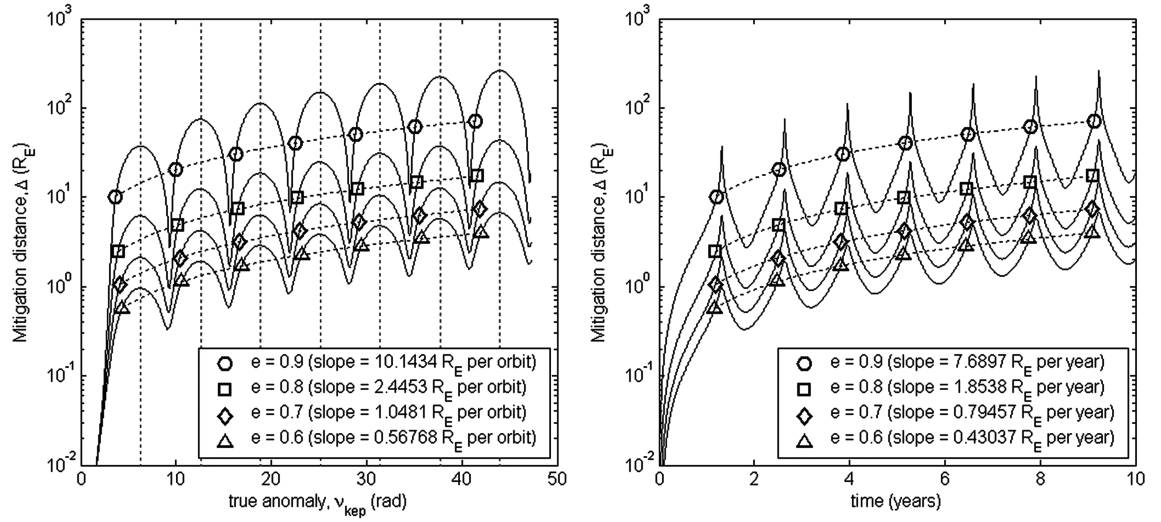

a) b)

Fig. 14 Effect of various orbit eccentricities vs a) true anomaly (angular) scale and b) time scale. All unspecified parameters correspond to the baseline case.

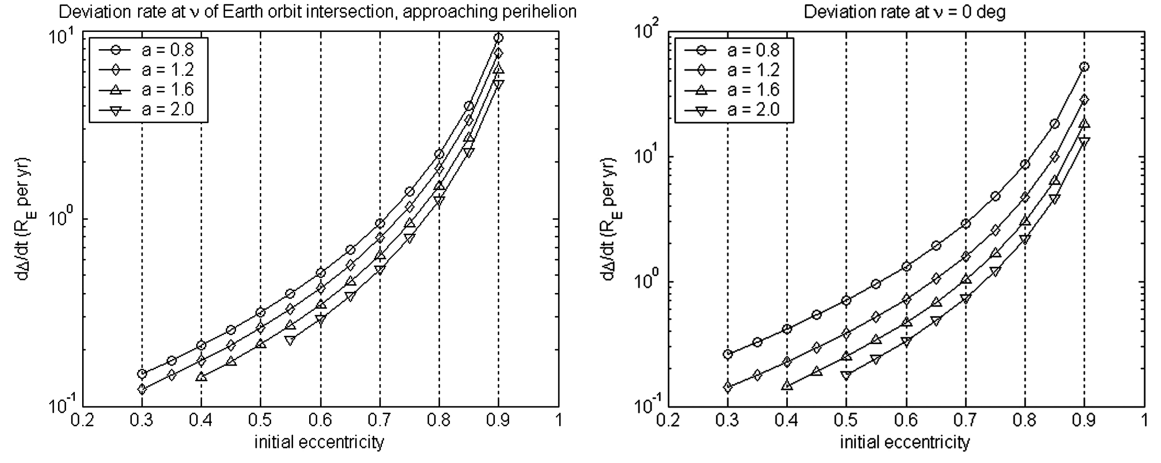

a) b)

Fig. 15 Effect of changing eccentricity on separation rate of change for a) true anomaly at which NEO orbit intersects Earth orbit approaching perihelion and b) true anomaly at perihelion All unspecified parameters correspond to the baseline case.

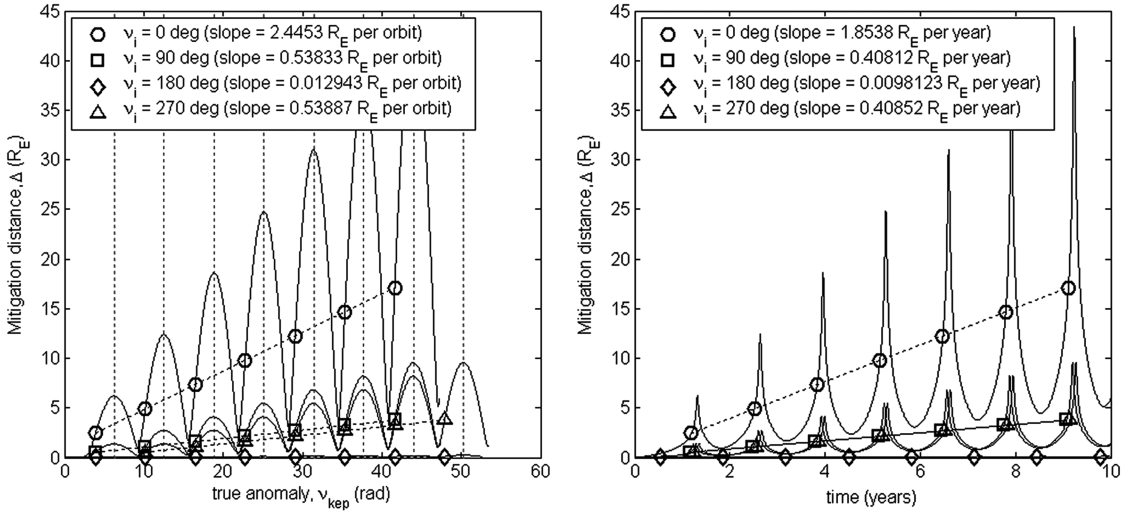

a) b)

Fig. 16 Effect of varying initial orbit true anomaly vs a) true anomaly (angular) scale and b) time scale. All unspecified parameters correspond to the baseline case.

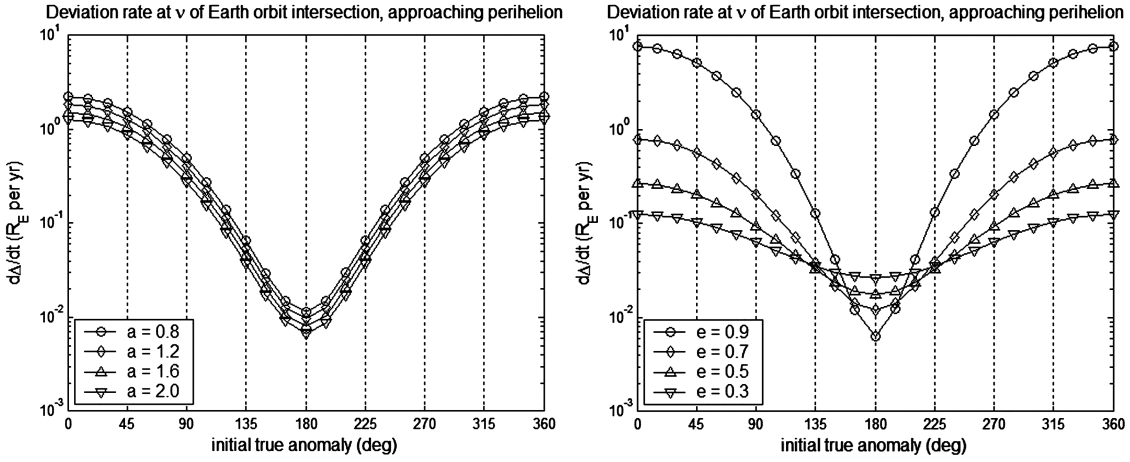

a) b)

Fig. 17 Parametric view of separation rates vs initial true anomaly plotted for various a) semimajor axes and b) eccentricities All unspecified parameters correspond to the baseline case.

The rate decreases to a minimum at 180 deg (apoapsis) and then returns to a maximum as it approaches perihelion again. These plots demonstrate that the best true anomaly for attachment is periapsis.

An explanation of this can be derived from examining the specific mechanical energy at the time of tether–ballast attachment. Determining the total energy before attachment is straightforward:

$$E_1 = \frac{1}{2}m_A(\dot{R}^2 + R^2\dot{\nu}^2) - \frac{m_A\mu_{\text{sun}}}{R} \tag{45}$$

Assuming the attachment of the tether and ballast mass is always performed with the tether pointing radially away from the sun ($\theta = 0$, this assumption will be proven to be beneficial later) and that the tether is rotating at exactly the rate of change of the true anomaly $\dot{\nu}$ at that time ($\dot{\theta} = 0$; more effective rotation rates exist, but this is assumed for simplicity), the position vector to the center of mass of the system after tether attachment can be calculated as follows:

$$\mathbf{R}_2 = \left(R + \frac{\tilde{m}L}{1+\tilde{m}}\right)\mathbf{a}_1 \tag{46}$$

Therefore, velocity can be determined (refer back to Fig. 1 for unit vector definition):

$$\mathbf{V}_2 = \dot{R}\mathbf{a}_1 + \left(R + \frac{\tilde{m}L}{1+\tilde{m}}\right)\dot{\nu}\mathbf{a}_2 \tag{47}$$

From this, kinetic and potential energies are found:

$$T_2 = \frac{1}{2}(m_A + m_B)\left[\dot{R}^2 + \left(R + \frac{\tilde{m}L}{1+\tilde{m}}\right)^2\dot{\nu}^2\right] \tag{48}$$

$$U_2 = -\frac{(m_A + m_B)\mu_{\text{sun}}}{R + [\tilde{m}L/(1+\tilde{m})]} \tag{49}$$

Combining the kinetic and potential energies yields the total energy:

$$E_2 = \frac{1}{2}(m_A + m_B)\left[\dot{R}^2 + \left(R + \frac{\tilde{m}L}{1+\tilde{m}}\right)^2\dot{\nu}^2\right] - \frac{(m_A + m_B)\mu_{\text{sun}}}{R + [\tilde{m}L/(1+\tilde{m})]} \tag{50}$$

Dividing Eqs. (45) and (50) by the total mass of each system [m_A for Eq. (45) and $m_A + m_B$ for Eq. (50)] results in equations describing the specific mechanical energies for both the unattached ϵ_1 and attached ϵ_2 systems:

$$\epsilon_1 = \frac{1}{2}(\dot{R}^2 + R^2\dot{\nu}^2) - \frac{\mu_{\text{sun}}}{R} \tag{51}$$

$$\epsilon_2 = \frac{1}{2}\left[\dot{R}^2 + \left(R + \frac{\tilde{m}L}{1+\tilde{m}}\right)^2 \dot{\nu}^2\right] - \frac{\mu_{\text{sun}}}{R + [\tilde{m}L/(1+\tilde{m})]} \tag{52}$$

Subtracting Eq. (51) from Eq. (52) reveals the difference in the specific mechanical energy between the two systems:

$$\Delta\epsilon = \epsilon_2 - \epsilon_1 = \frac{\tilde{m}L\dot{\nu}^2}{1+\tilde{m}}\left(R + \frac{\tilde{m}L}{2+2\tilde{m}}\right) + \mu_{\text{Sun}}\left(\frac{1}{R} - \frac{1+\tilde{m}}{R + R\tilde{m} + \tilde{m}L}\right) \tag{53}$$

Figure 18 illustrates this difference vs the true anomaly at which the attachment is made. For Fig. 18a, several values of semimajor axis are shown, and for Fig. 18b, various eccentricities are shown.

Figure 18 is similar to Fig. 17 and confirms that more energy is gained for an attachment at periapsis than at any other point in the orbit, regardless of orbit size and shape. Note that although they are not shown here, various values of L and m_A:m_B were also plotted and examined. These plots showed that the gains in energy were approximately proportional to the changes in length or mass ratio, but periapsis attachment still resulted in the largest energy gain.

G. Effect of Initial Tether Angle

In Fig. 19, the effect of varying the initial tether angle is shown. The figure appears not to include the $\theta = 0$ deg case, but it is almost indistinguishable from the $\theta = 180$ deg case, and so the plots overlap. These two cases clearly outperform the $\theta = 90$ and 270 deg cases.

The reason for this phenomenon is that if the initial tether angle is at 90 or 270 deg, the new center of mass is in the same orbit as the original NEO. Attaching at 0 or 180 deg maximizes the instantaneous change in the perihelion distance of the system. It is also interesting to note the oscillation seen in the $\theta_i = 90$ and 270 deg cases. This shows the small-scale effects of the rotation of the NEO–tether–ballast system about its center of mass.

Figure 20 shows a parametric view of separation rates as a function of initial tether angle. The maximum separation rates occur for tethers at right angles to the local horizontal. As the tether angle aligns with the local horizontal, the rate approaches zero. Overall, this plot demonstrates that tether angles of 0 and 180 deg at attachment are the most advantageous for trajectory alteration.

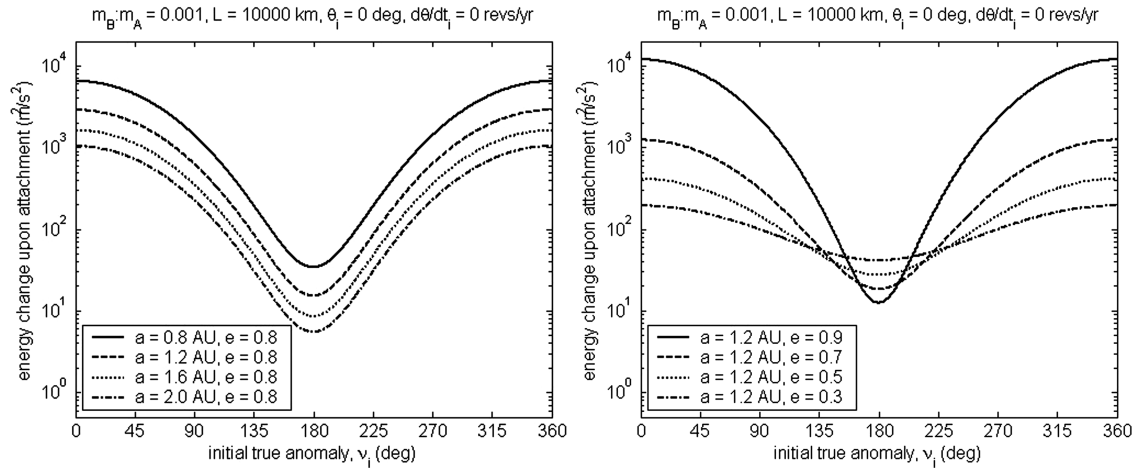

a) b)

Fig. 18 Gain in specific mechanical energy, $\epsilon_2 - \epsilon_1$, varying a) semimajor axis, a, and b) eccentricity, e.

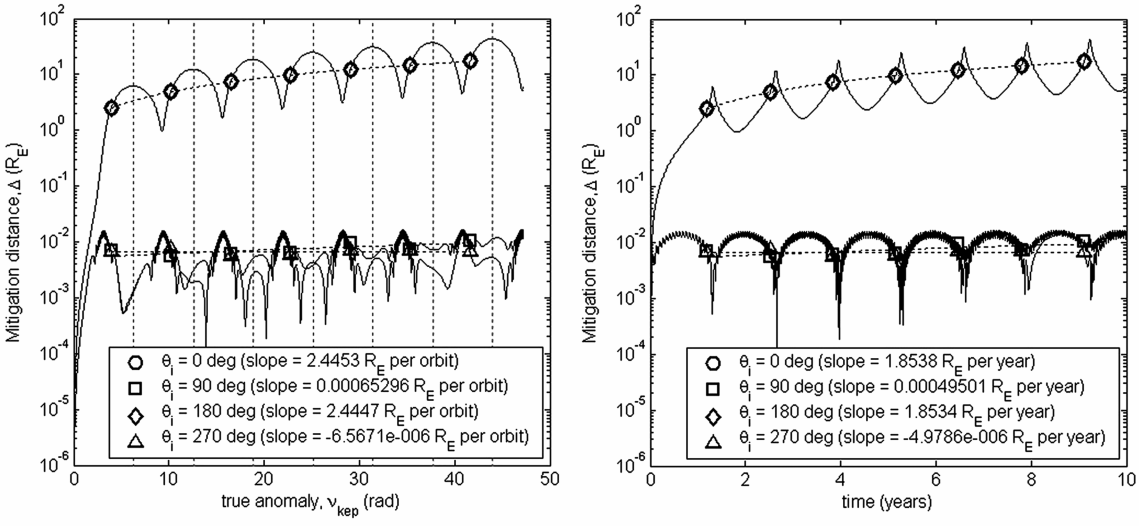

a) b)

Fig. 19 Effect of varying initial tether angle vs a) true anomaly (angular) scale and b) time scale. All unspecified parameters correspond to the baseline case.

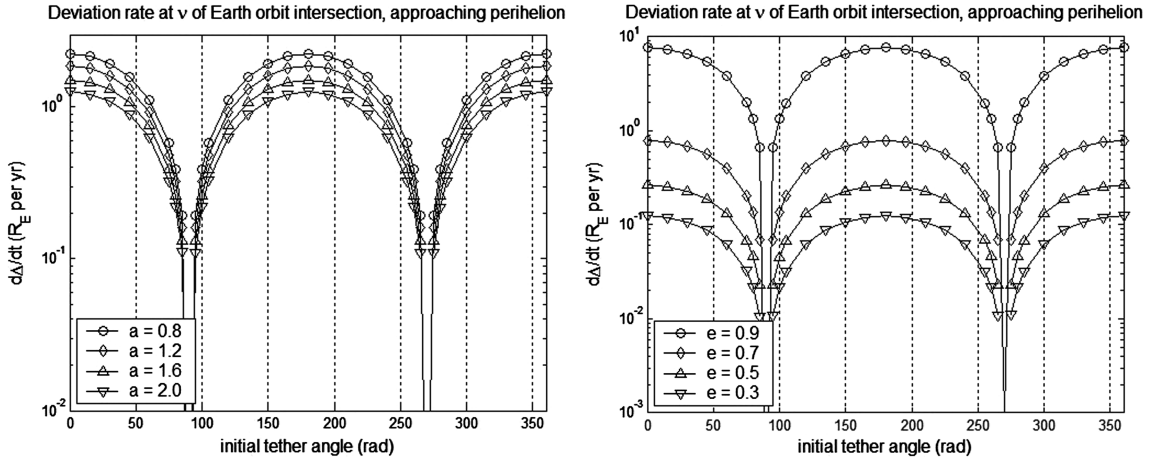

a) b)

Fig. 20 Parametric view of separation rates vs initial tether angle for orbits of various a) semimajor axes and b) eccentricities. Unspecified parameters are baseline values.

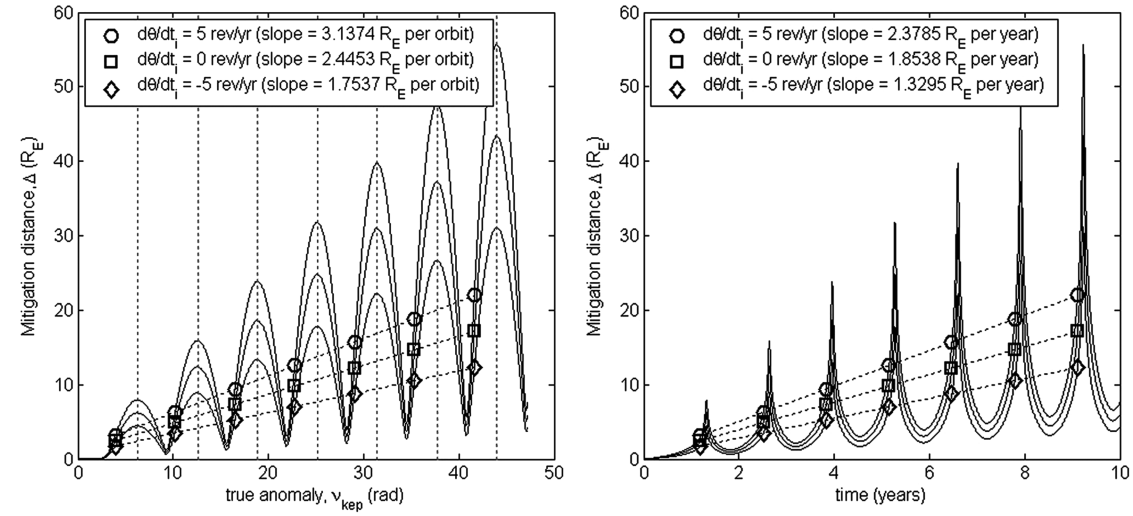

a) b)

Fig. 21 Effect of varying initial tether angle rotation rate vs a) true anomaly (angular) scale and b) time scale. All unspecified parameters correspond to the baseline case.

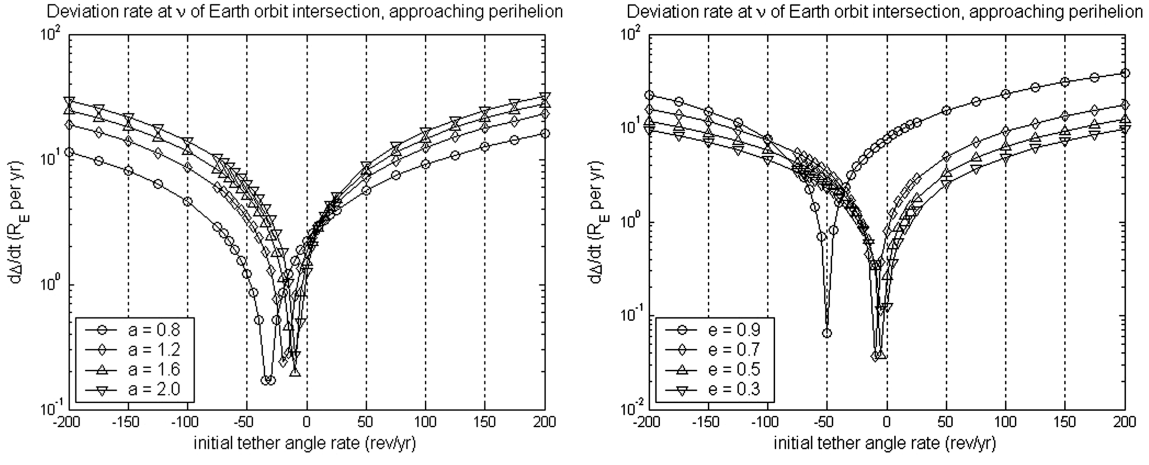

a) b)

Fig. 22 Parametric view of separation rates vs tether rotation rate for orbits of various a) semimajor axes and b) eccentricities. Unspecified parameters are baseline.

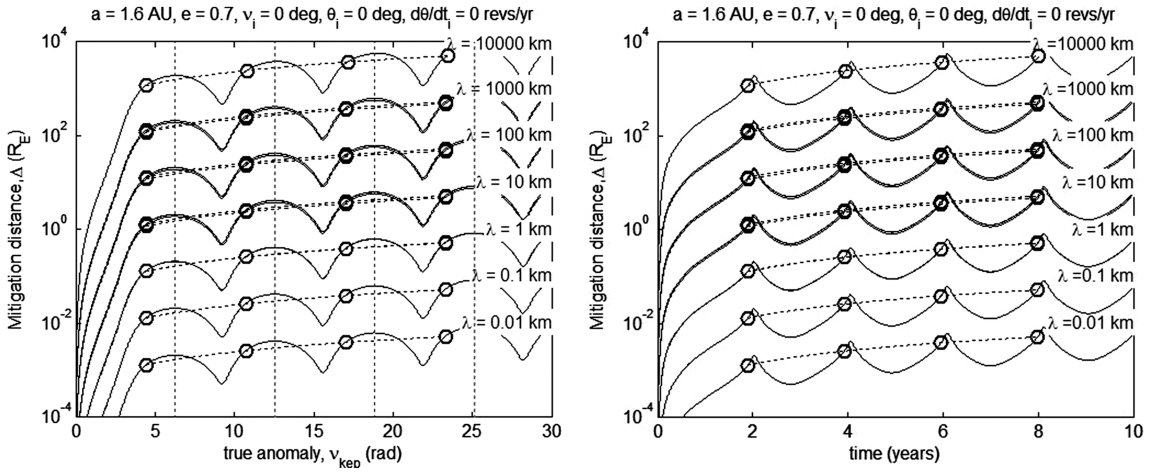

a) b)

Fig. 23 Plot of 16 cases showing approximate equivalence of equal λ cases vs a) true anomaly (angular) scale and b) time scale.

Although the plots in Fig. 20 clearly do not span the entire *a–e* parametric space, they are representative of the entire Earth-orbit-crossing space regarding the advantage of these attachment configurations.

H. Effect of Initial Tether Angle Rotation Rate

There are logistical reasons that an initial tether rotation rate of 0 is preferable, but variations from this are interesting. By increasing this rate in the direction of increasing true anomaly, the system center of mass is accelerated, increasing the system center of mass velocity at perihelion, resulting in a higher-energy orbit and greater separation.

On the other hand, a slight decrease from a zero rate has a detrimental effect on performance, as Fig. 21 shows. However, Fig. 22 shows that this is only true for small negative rates. For larger negative rotation rates, separation performance is similar to large positive rates.

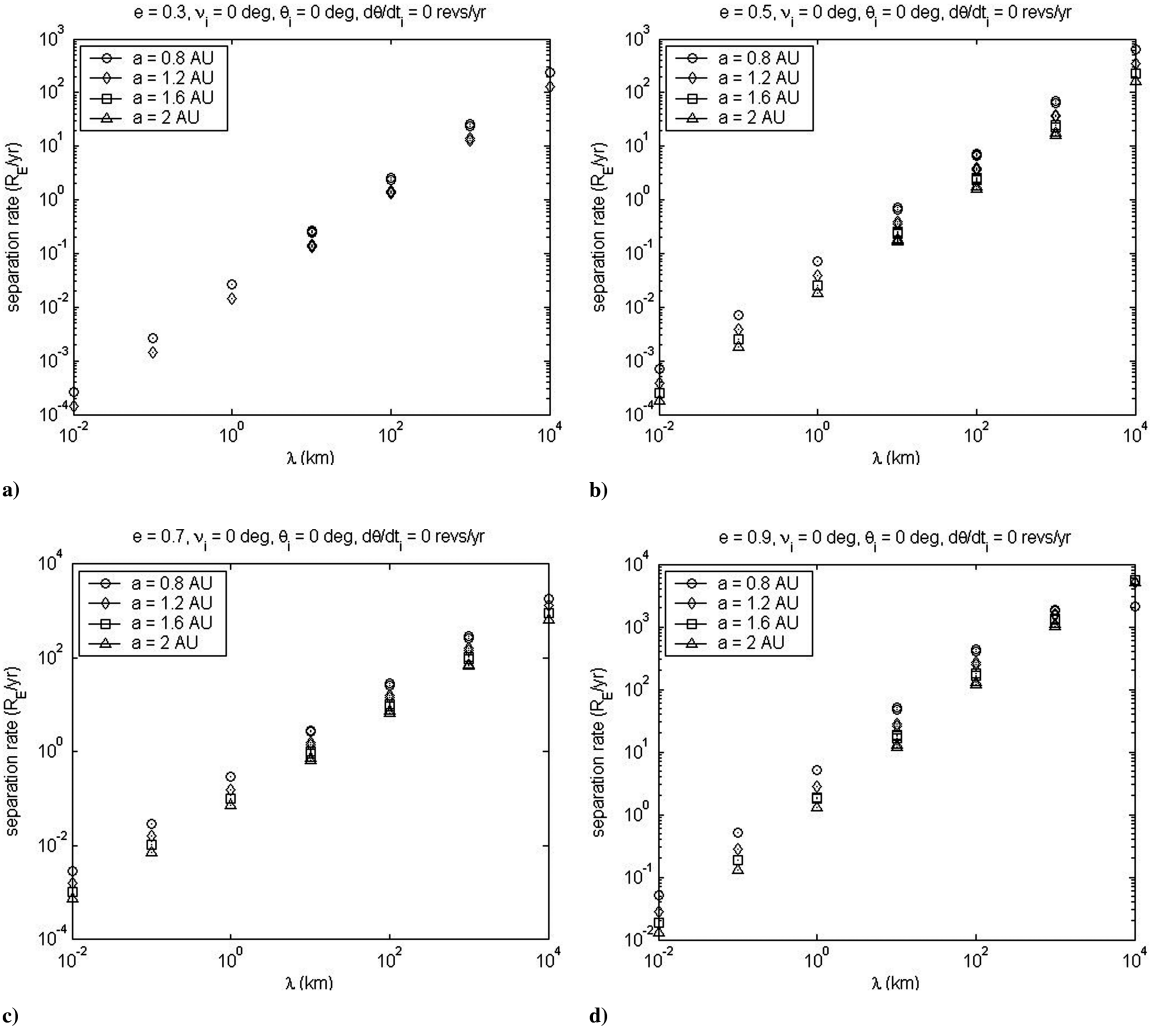

a) b) c) d)

Fig. 24 Parametric plot of separation rates vs λ for a) $e = 0.3$, b) $e = 0.5$ c) $e = 0.7$, and d) $e = 0.9$.

Figure 22 shows the effect of the tether rotation rate on the separation rate. This chart shows that either a positive or a negative rotation can improve separation rates. For each case, though, there is a minimum performance region near, but less than, 0.

In spite of these results, it is assumed that were a tether mitigation attempted, it would most likely involve a nonrotating tether to maximize the chance of successful deployment. Therefore, the baseline examples in this study assume a zero tether rotation rate at the time of attachment.

I. Summary of Parametric Results

As stated earlier, any equivalent product of mass ratio $\tilde{m}$ and tether length L will produce approximately the same separation over time. We therefore define a new parameter λ:

$$\lambda = \tilde{m}L \tag{54}$$

Any two cases in which the value of λ is the same will have very similar results. For example, the case of a mass ratio of 0.01 and a tether length of 10,000 km will produce the same result as a mass ratio of 0.1 and a tether length of 1000 km. Figure 23 demonstrates this for 16 cases that fall into seven approximately equivalent plots.

To create the plots, all possible combinations of the mass ratio parameters (0.1, 0.01, 0.001, and 0.0001) and the tether length parameters (100, 1000, 10,000, and 100,000 km) were plotted. Specifically, the $\lambda = 10,000$ km case is a single case combining $\tilde{m}$ of 0.1 and L of 100,000 km. The $\lambda = 1000$ km case is composed of two cases: $\tilde{m}$ of 0.1 with L of 10,000 km and $\tilde{m}$ of 0.01 with L of 100,000 km. In a similar manner, the $\lambda = 100$ km case is composed of three combinations, $\lambda = 10$ km is composed of four, $\lambda = 1$ km is composed of three, $\lambda = 0.1$ km is composed of two, and $\lambda = 0.01$ km is composed of one combination.

Figures 24 and 25 show parametrically how the separation rates vary for different values of λ as well as for different orbit sizes and shapes. As in Fig. 23, all combinations of mass ratio and tether length were plotted with repeated values of λ. Thus, these plots reinforce that for a particular value of λ, the separation rates overlap (all identical markers for each value of λ are approximately equal). Again, the purpose of these plots is to convince the reader of the validity of compressing $\tilde{m}$ and L into a single variable λ for the purpose of summary. Moreover, they help support the claim that this is true over the entire a–e parametric space.

Figure 26 gives a summary of the separation distance rates $\dot{\Delta}$ for different values of a, e, and λ. The eccentricity is represented on the x axis, the semimajor axis is represented on the y axis, and the separation distance slopes are plotted on the z axis. The extent of each mesh (a–e parametric space spanned by each value of λ) reflects the values of a and e for which an intersection with the Earth's orbit is possible. Note that each increase in λ, where $\lambda = \tilde{m}L$, results in a proportional increase in separation distance rate of change over time, $\dot{\Delta}$.

J. Case Study

To reinforce the conclusions of this paper, a case study is now presented. The scenario involves a near-Earth object that needs to be deflected from its current trajectory. The orbital elements for the NEO include a semimajor axis of 1.2 AU and an eccentricity of 0.8. The tether length will be limited to 10,000 km and the mass ratio will

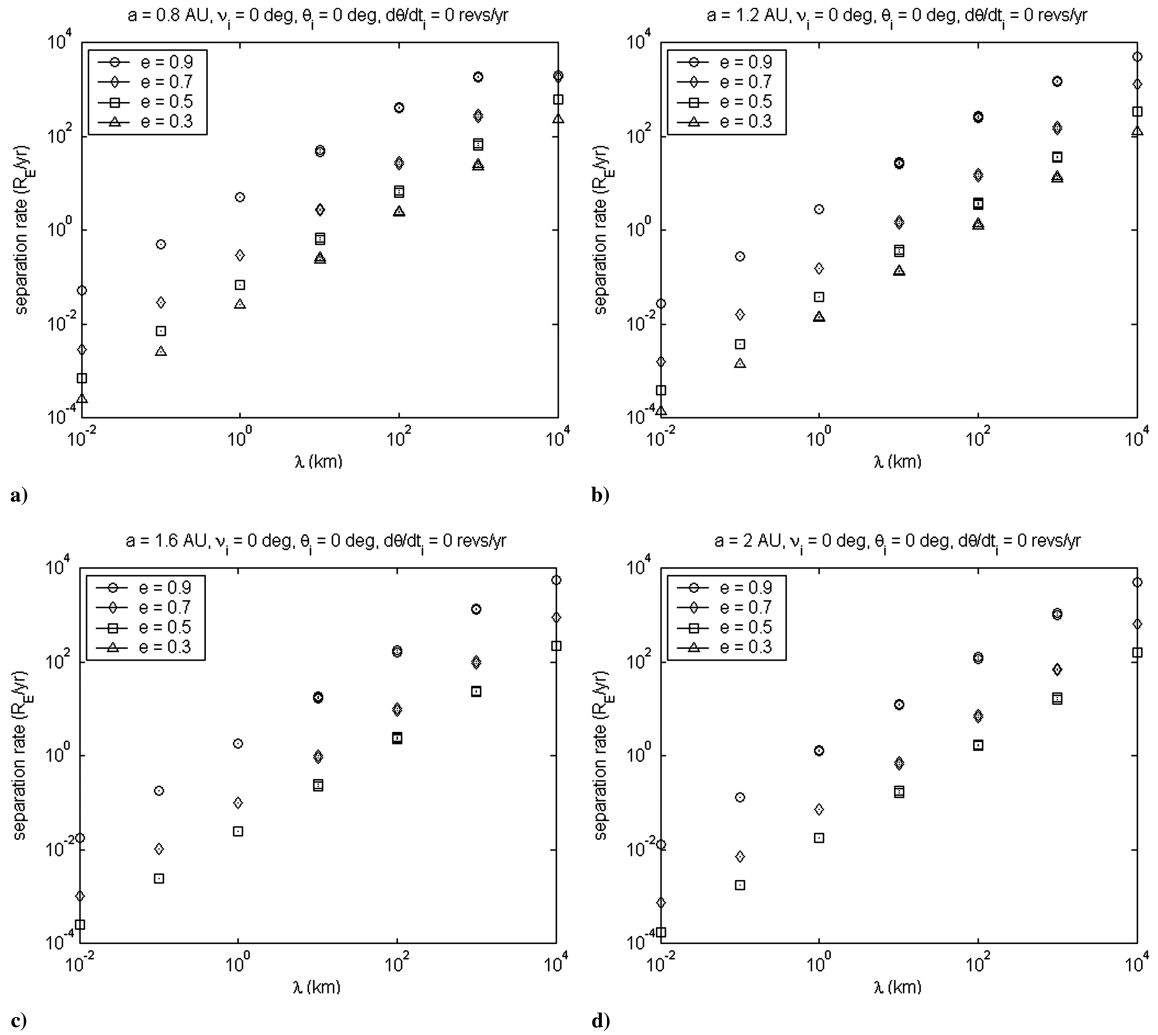

Fig. 25 Parametric plot of separation rates vs λ for a) $a = 0.8$, b) $a = 1.2$ c) $a = 1.6$, and d) $a = 2.0$.

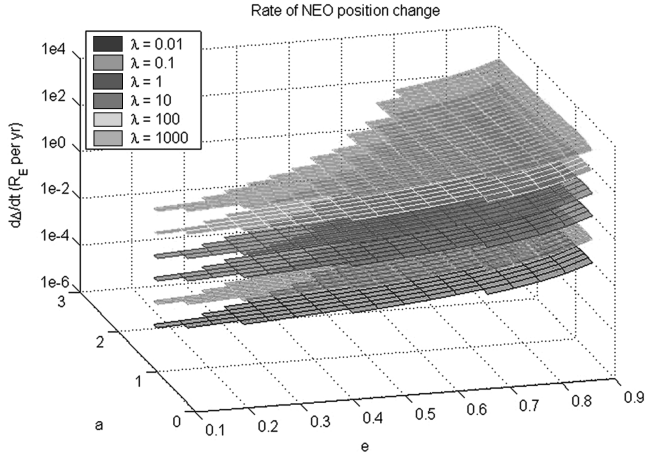

Fig. 26 Summary of results using slope of separation curve vs semimajor axis and eccentricity of NEO orbits.

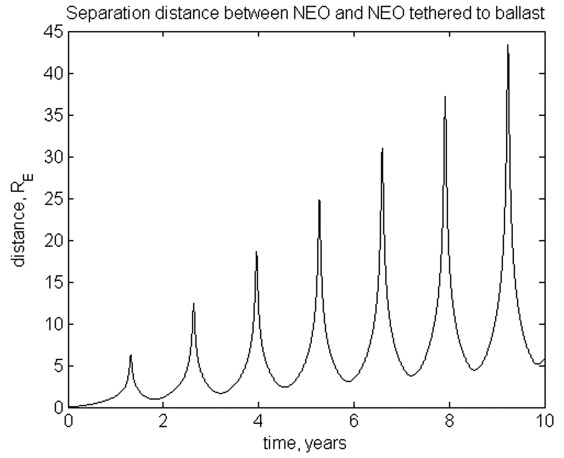

Fig. 27 Time history of separation between NEO and the same NEO tethered to a ballast mass.

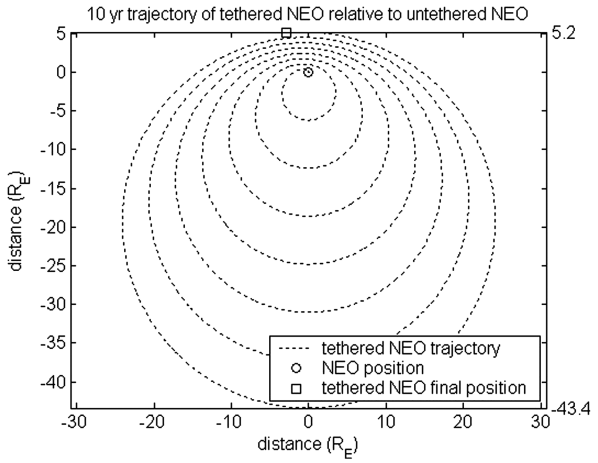

Fig. 28 Relative trajectory of a NEO tethered to a ballast mass with respect to the same NEO's position if untethered.

be limited to 0.1% of the NEO mass. This case study is aligned with the baseline parameters given earlier. Given this scenario, two plots were created. Figure 27 shows the time history of the scalar separation distance between a NEO and the same NEO tethered to a ballast mass. Figure 28 was created to show the trajectory of the tethered NEO relative to the untethered NEO. It can be seen from both figures that after 10 years, there is a significant alteration of the trajectory of approximately 6 Earth radii after 10 years. Additionally, a separation of one Earth radius was achieved by the third year.

V. Conclusions

This study demonstrates the potential effectiveness of using the attachment of a tether and ballast mass to a near-Earth object (NEO) to alter its trajectory. The design parameters and orbit size and shape impact the effectiveness. The tether length and the mass ratio between the ballast and the NEO both directly affect the new location of the system center of mass after tether and ballast mass connection. Changes in either of these parameters result in a proportional change in the trajectory separation rate $\dot{\Delta}$ over time. The effect of orbit size and shape (semimajor axis and eccentricity) can be summarized as follows: smaller, more elliptical, orbits are more responsive to tether–ballast mitigation than larger, more circular, orbits. For orbit size (specifically, semimajor axis), this generalization is limited. Below a certain value of semimajor axis, depending on the point in the orbit at which the deviation rate is calculated, the deviation rate begins to decrease with decreasing orbit size. The best point in the orbit (defined in this paper by true anomaly ν) at which the tether should be connected to the NEO is periapsis. This results in a maximum deviation for a given NEO–tether–ballast configuration. Given the results of this parametric study, it is believed that the use of a tether and ballast mass shows promise as a mitigation technique. This is especially true for cases that fall within the advantageous parametric space described previously.

Appendix A: Convergence

To demonstrate the necessity for using Encke's method in this study, some results demonstrating the differences in convergences between Encke's and Cowell's methods will now be presented.

The discussion must begin by defining convergence. For this study, it means that *nearly* the same result (final position of the NEO in this case) is achieved, given a slight variation in some parameter of a numerical integration scheme. Often in convergence testing, the time step is the varied parameter. In this case, using the time step is prohibitive, and so the tolerances of MATLAB's ordinary differential equation (ODE) solver suite are used instead. Specifically, MATLAB's ODE suite uses two separate error-tolerance schemes: relative tolerance and absolute tolerance. The two combine to determine how much estimated error is acceptable to the ODE solver. Equation (A1) defines this relationship [15]. In this equation, E_i is the allowable estimated error for y_i, the ith component of the state vector; r is the relative error; and a_i is the absolute error for the ith component:

$$|E_i| \leq r|y_i| + a_i \tag{A1}$$

It is reasonable to assume that if the results of a numerical integration are valid, then a slight decrease in the allowable error E_i, resulting in slightly stricter tolerances, should produce nearly the same result. This method of convergence testing was used to determine the degree to which all cases converged, specifically showing that decreasing ODE solver tolerances resulted in closer and closer final positions of the NEOs.

Figure A1 demonstrates the difference between the rate of convergence of the Cowell and Encke methods. The figure title specifies the parameters for the case (5-year simulation, semimajor axis of 1.2 AU, orbital eccentricity of 0.8, tether length of 100,000 km and ballast-to-NEO mass ratio of 0.1). Along the x axis is the log of the `dfac`, which is the base 10 logarithmic value of the denominator for both the relative tolerance and the absolute tolerance vector. More precisely, it is the log of the lesser of two results in which `dfac` is varied. For example, the particular point shown above the x-axis value of 3 represents the scalar position difference resulting from a `dfac` of 10^3 and a `dfac` of 10^4. Likewise, the values shown above the x-axis value of 4 are the difference between tolerances resulting from a `dfac` of 10^4 and a `dfac` of 10^5, and so on. Therefore, the scale ranges by orders of magnitude from a minimum `dfac` of 10^3 (difference between `dfac` cases of 10^4 and 10^3) to a maximum of

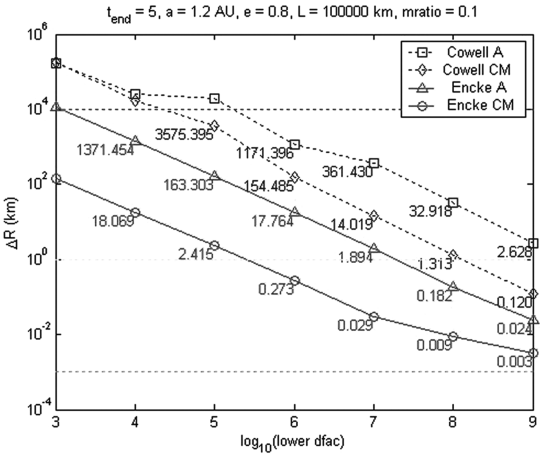

Fig. A1 Difference in rates of convergence for the Cowell and Encke methods.

10^9 (difference between cases of 10^9 and 10^{10}). This scale provides a range of tolerances that vary from, at the low end, 1×10^{-3} (the default value of relative tolerance), and at the high end, 1×10^{-13}, nearly the smallest relative tolerance allowed by MATLAB's ODE suite (the minimum is 4×10^{-14}). On the y axis is the maximum difference in position as measured in Cartesian coordinates between two consecutive `dfac` values. The legend describes four cases: Encke A shows the convergence of the NEO position and Encke CM shows the convergence of the NEO–tether–ballast system center of mass. Likewise, Cowell A and Cowell CM show these cases for Cowell's method. It can then be seen that convergence is reached for lower values of `dfac` for the Encke's method cases than for the Cowell's method cases. Although Encke's method turns out to be slightly more computationally expensive, taking slightly longer to generate than the Cowell's method cases, the gains realized in convergence make this method preferable to direct integration.

To demonstrate this, the analysis shown in Fig. A1 was conducted over a range of semimajor axes and eccentricities. The resulting plots shown in Fig. A2 demonstrate the level of convergence. In this plot, the x axis consists of a range of eccentricity values and the y axis consists of a range of semimajor-axis values. The legend specifies the level of convergence. Also included in the background is a chart showing the parametric density of potentially hazardous asteroids (see footnote ‡) for those ranges, with the brighter areas indicating a higher parametric density. There are four charts, two that show relatively good convergence for Encke's method, and two showing poorer convergence performance for Cowell's method. For each method, there is a chart showing convergence at the NEO and another showing convergence at the system center of mass.

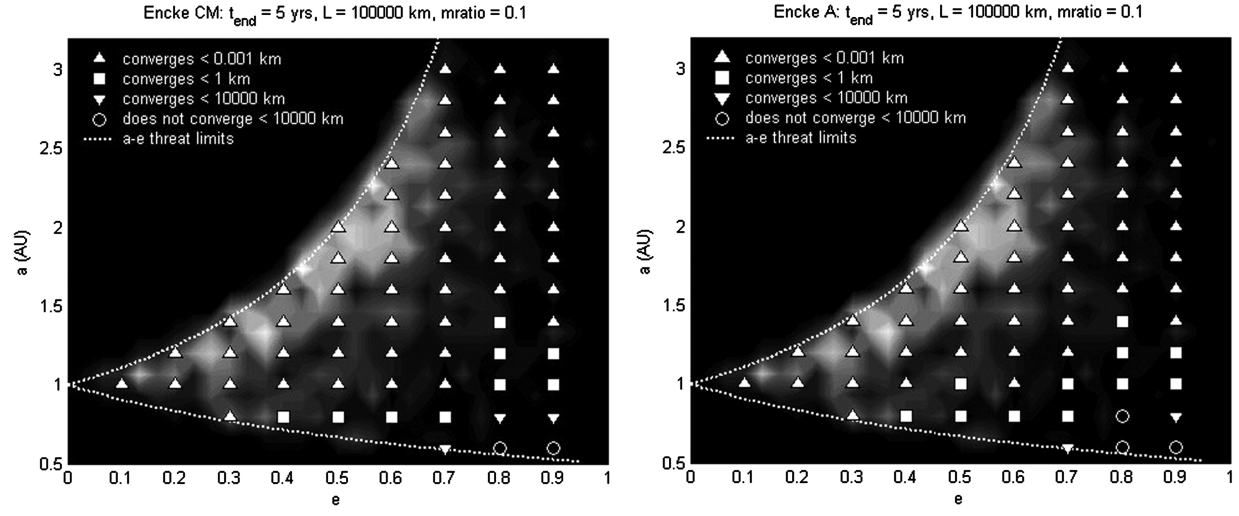

a)

b)

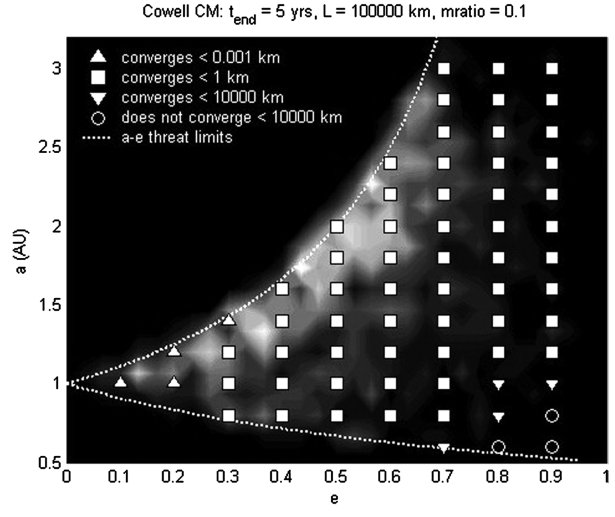

c)

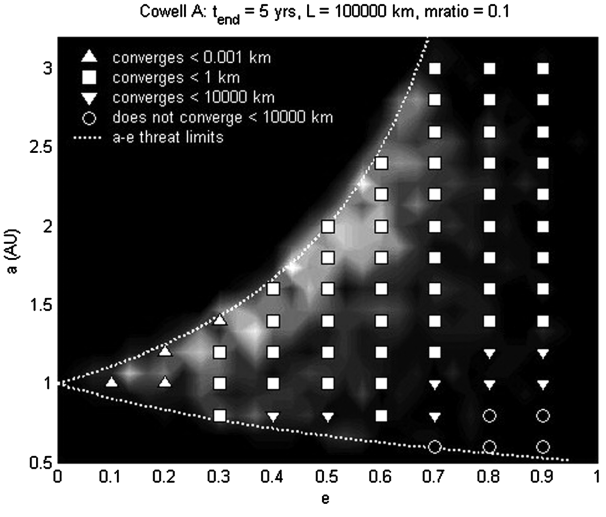

d)

Fig. A2 Convergence at a) center of mass, b) NEO, c) center of mass, and d) NEO.

The figure reinforces the value of using Encke's method for data generation. And in fact, Encke's method was used for all data generation leading to the results presented in this study.

References

[1] Grant, J. A., "Evaluating the Evolution of Process Specific Degradation Signatures Around Impact Craters," *International Journal of Impact Engineering*, Vol. 23, No. 1, Dec. 1999, pp. 331–340. doi:10.1016/S0734-743X(99)00084-6

[2] Alvarez, L. W., Asaro, F., Michel, H. V., and Alvarez, W., "Extraterrestrial Cause for the Cretaceous-Tertiary Extinction. Experimental Results and Theoretical Interpretation," *Science*, Vol. 208, No. 4448, June 1980, pp. 1095–1108. doi:10.1126/science.208.4448.1095

[3] Grieve, R., and Therriault, A., "Vredefort, Sudbury, Chicxulub: Three of a Kind?," *Annual Review of Earth and Planetary Sciences*, Vol. 28, 2000, pp. 305–338. doi:10.1146/annurev.earth.28.1.305

[4] Sansaturio, M. E., and Arratia, O., "Apophis: The Story Behind the Scenes," *Earth, Moon, and Planets*, Vol. 102, Nos. 1–4, June 2008, pp. 425–434. doi:10.1007/s11038-007-9165-3

[5] "Near-Earth Object Survey and Detection Analysis of Alternatives," Mar. 2007, http://neo.jpl.nasa.gov/neo/report2007.html [retrieved 14 Dec. 2007].

[6] Ahrens, J., and Harris, A. W., "Deflection and Fragmentation of Near-Earth Asteroids," *Nature*, Vol. 360, No. 6403, Dec. 1992, p. 429. doi:10.1038/360429a0

[7] McInnes, C. R., "Deflection of Near-Earth Asteroids by Kinetic Energy Impacts from Retrograde Orbits," *Planetary and Space Science*, Vol. 52, No. 7, June 2004, pp. 587–590. doi:10.1016/j.pss.2003.12.010

[8] Spitale, J. F., "Asteroid Hazard Mitigation Using the Yarkovsky Effect," *Science*, Vol. 296, No. 5565, Apr. 2002, p. 77. doi:10.1126/science.1069577

[9] Lu, E., "The Project B612 Concept," *2004 Planetary Defense Conference: Protecting Earth from Asteroids*, AIAA, Reston, VA, 2004, pp. 130–131.

[10] Lu, E. T., and Love, S. G., "Gravitational Tractor for Towing Asteroids," *Nature*, Vol. 438, No. 7065, Nov. 2005, pp. 177–178. doi:10.1038/438177a

[11] Chobotov, V. A., and Melamed, N., "Deflection of Near Earth Objects by Means of Tethers," *2007 Planetary Defense Conference Invited Presentations and Papers*, Aerospace Corp., Washington, D.C., Mar. 2007, http://www.aero.org/conferences/planetarydefense/2007papers/P2-7--Chobotov-Brief.pdf [retrieved 14 Dec. 2007].

[12] MATLAB, Software Package, Ver. 6.5, Release 13, The Mathworks, Inc., Natick, MA, June 2002.

[13] Modi, V. J., and Misra, A. K., "Orbital Perturbations of Tethered Satellite Systems," *Journal of the Astronautical Sciences*, Vol. 25, No. 3, July–Sept. 1977, pp. 271–278.

[14] Bate, R. R., Mueller, D. D., and White, J. E., *Fundamentals of Astrodynamics*, Dover, New York, 1971.

[15] Shampine, L. F., and Reichelt, M. W., "The MATLAB ODE Suite," *SIAM Journal on Scientific Computing*, Vol. 18, No. 1, Jan. 1997, pp. 1–22. doi:10.1137/S1064827594276424

D. Spencer
Associate Editor